Cortical F-actin stabilization generates apical–lateral patterns of junctional contractility that integrate cells into epithelia

Selwin K. Wu[1], Guillermo A. Gomez[1,4], Magdalene Michael[1], Suzie Verma[1], Hayley L. Cox[1], James G. Lefevre[2], Robert G. Parton[1], Nicholas A. Hamilton[1,2], Zoltan Neufeld[3] and Alpha S. Yap[1,4]

E-cadherin cell–cell junctions couple the contractile cortices of epithelial cells together, generating tension within junctions that influences tissue organization. Although junctional tension is commonly studied at the apical zonula adherens, we now report that E-cadherin adhesions induce the contractile actomyosin cortex throughout the apical–lateral axis of junctions. However, cells establish distinct regions of contractile activity even within individual contacts, producing high tension at the zonula adherens but substantially lower tension elsewhere. We demonstrate that N-WASP (also known as WASL) enhances apical junctional tension by stabilizing local F-actin networks, which otherwise undergo stress-induced turnover. Further, we find that cells are extruded from monolayers when this pattern of intra-junctional contractility is disturbed, either when N-WASP redistributes into lateral junctions in H-Ras^V12-expressing cells or on mosaic redistribution of active N-WASP itself. We propose that local control of actin filament stability regulates the landscape of intra-junctional contractility to determine whether or not cells integrate into epithelial populations.

Cadherin-based cell–cell junctions are mechanical connections, actively coupling and integrating the force-generating cortices of neighbouring cells together[1–5]. These reciprocal interactions generate junctional tension[6,7] that influences tissue organization[8–10]. In addition, contractile interactions across junctions can affect how cells integrate into tissues. This is strikingly illustrated by the process of cell extrusion, where normal cells that surround apoptotic or oncogene-transfected cells exert forces on those heterologous contacts to expel them from the monolayer[11–13]. This further implies that the impact of contractile forces acting on cell–cell junctions can influence whether or not cells integrate into epithelia.

At the cellular level, junctional tension arises from dynamic interactions between the cadherin adhesion system and the contractile actomyosin cytoskeleton[14]. These interactions are best understood for the epithelial zonula adherens, a specialized junction where E-cadherin (also known as CDH1) concentrates with actin and myosin II to form a contractile ring[7,15]. The actomyosin apparatus at the zonula adherens reflects integration of cadherin-based actin assembly, mediated by the WAVE2–Arp2/3 nucleator[16,17], with cadherin-based signalling that supports the junctional recruitment of active myosin II (refs 7, 15,18). Apical junction tension is compromised when any of these elements are disrupted.

The zonula adherens is not the only region where cadherins engage in adhesion[19–25]. However, the contractile properties of cadherin junctions away from the zonula adherens, and how they may relate to those of the zonula adherens, are not known. In this study we find that all regions of cadherin adhesion in epithelial cells interact with the contractile actomyosin cortex. However, epithelial junctions establish disparate levels of contractile tension at apical and lateral zones that coexist even within individual contacts. These patterns of intra-junctional contractility reflect differences in the local stability of cortical F-actin, and influence the integration of cells into monolayers.

RESULTS

Distinct levels of tension coexist within individual E-cadherin junctions

E-cadherin junctions couple with cortical actomyosin to generate forces between cells[2,26]. In confluent Caco-2 cells, E-cadherin accumulates in an apical ring, corresponding to the zonula adherens[27,28], which associates with circumferential actomyosin bundles[15,29] (Fig. 1a) to generate tension[7]. Visualization of *en face* contacts (Supplementary Fig. 1a) showed that cadherin puncta also distribute throughout the lateral junctions below the zonula adherens, often forming apparent
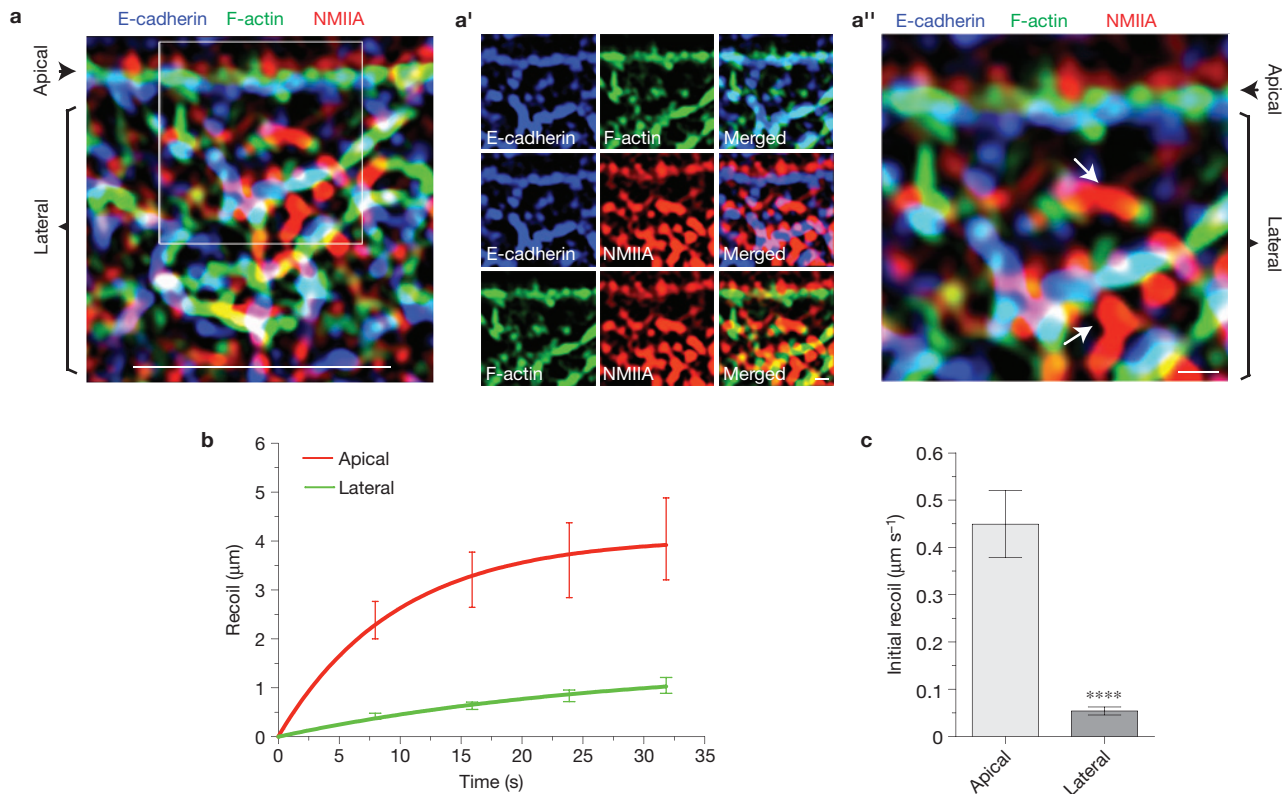
Figure 1 Distinct levels of contractile tension coexist within individual E-cadherin junctions. (**a**) Cortical F-actin (GFP–UtrCH), non-muscle myosin heavy chain IIA (NMIIA, also known as MYH9) and E-cadherin at apical (zonula adherens) and lateral zones of cell–cell junctions. (**a'**,**a"**) Detailed views of the indicated area in **a**. Arrows identify myosin-bridging actin cables.

(**b**,**c**) Best-fit single exponential curves of apical and lateral junctional recoil (**b**) and tension (initial recoil, **c**) following nanoablation. Data are means ± s.e.m., ****$P < 0.0001$; calculated from $n = 3$ independent experiments analysed by nonlinear regression (statistical information and source data in Supplementary Table 1). Scale bars, 5 μm (**a**), 0.5 μm (**a'**,**a"**).

nodes for a network of short actin cables decorated and connected by myosin II (Fig. 1a and Supplementary Figs 1b and 3a). The lateral junctions, then, were also decorated by an actomyosin cortex. As it is unclear whether the zonula adherens and lateral junctions have similar or distinct contractile properties, we used two-photon laser nanoscissors[30] to focally ablate these regions. Instantaneous recoil of cadherin clusters from the cut site indicated the presence of local junctional tension, both at the zonula adherens and within lateral junctions (Fig. 1b,c and Supplementary Fig. 1c,d and Video 1). However, initial recoil was significantly faster at the zonula adherens, demonstrating that substantial differences in tension exist even within individual junctions. We then sought to understand how such apico-lateral patterns of contractility could be generated.

E-cadherin puncta represent adhesive clusters

A possible explanation for this regional disparity was that the zonula adherens and lateral junctions represented segregated cadherin populations. However, this was not the case, as E-cadherin (Ecad)–PA-GFP (photoactivatable green fluorescent protein) signals appeared in the zonula adherens after lateral photoactivation and vice versa (Fig. 2a–d and Supplementary Video 2). Nor did the lateral puncta represent intracellular vesicles incapable of engaging in adhesion. E-cadherin was predominantly at the cell surface (Supplementary Fig. 2a) and the lateral clusters did not label with endosomal markers

such as internalized transferrin (Fig. 2e), a FYVE-domain reporter (Fig. 2f and Supplementary Video 3) or caveolin (Supplementary Fig. 4a and Video 4). Further, three-dimensional co-localization analysis[31] demonstrated that ~70–80% of puncta at the interface between cells expressing either Ecad–GFP or Ecad–tdTomato (Ecad–tdT) incorporated both fluorophores (Fig. 2g,h and Supplementary Fig. 2b), indicative of *trans*-interactions. Thus, most puncta represented adhesive clusters, rather than intracellular vesicles, which would be predicted to incorporate only one fluorophore.

Motion analysis identifies functional coupling of contractility to cadherin clusters

Another possibility was that lateral cadherin clusters were not physically coupled to the contractile apparatus[32,33]. To test this we interrogated the planar motion of Ecad–GFP clusters in videos of *en face* contacts by particle velocity tracking[34] and Fourier analysis[35] (Fig. 3a–d and Supplementary Fig. 2d and Video 5). Whereas clusters within the zonula adherens underwent slow unidirectional displacement[35], lateral puncta exhibited marked, quasi-oscillatory, movements (period ~ 111 s) with a power spectrum amplitude at the principal frequency ~5-fold greater than that at the zonula adherens (Fig. 3b–d). Correlation time-lapse analysis of puncta formed between cells expressing either Ecad–GFP or Ecad–tdT confirmed that these were adhesive clusters that moved together as co-localized spots (Fig. 3e and Supplementary Fig. 2f and
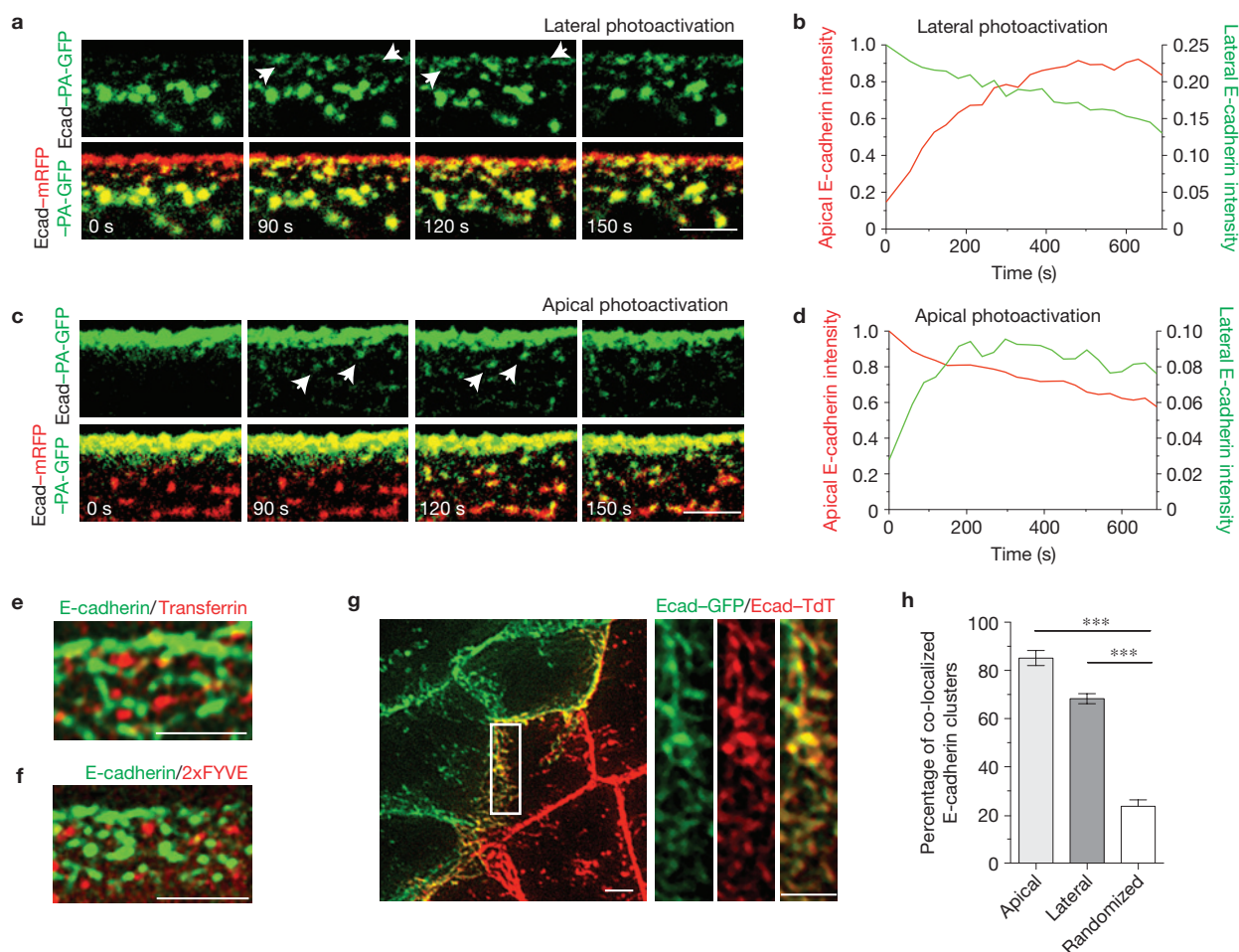
Figure 2 E-cadherin clusters exchange between the apical and lateral junctions. (**a**–**d**) Ecad–mRFP–PA-GFP (Ecad, E-cadherin; mRFP, monomeric red fluorescent protein) exchanges between the zonula adherens and lateral junction. Time-lapse images and mean regional fluorescence intensity following selective photoactivation in the lateral (**a**,**b**) or apical (**c**,**d**) zones of junctions; data are representative of 3 independent experiments. (**e**,**f**) Ecad–GFP clusters at junctions do not co-localize with either internalized transferrin (**e**) or a 2xFYVE reporter (**f**). (**g**) Cadherin clusters at the interface between cells expressing either Ecad–tdT or Ecad–GFP with detailed views (right). (**h**) Co-localization quantified at the apical and lateral junctions was compared with randomized image stacks of the lateral junctions. Data are means $\pm$ s.e.m., ***$P < 0.001$; $n = 4$ independent experiments with one-way ANOVA, Dunnett's *post hoc* test (statistical information and source data in Supplementary Table 1). Scale bars, 5 µm.

Video 6). Clusters also underwent oscillatory movements orthogonal to the junctions, without net constriction of the lateral domains (Fig. 3f). These data suggested that oscillations reflected contractile activity from both sides of a cell–cell contact acting on adhesive clusters. Indeed, lateral oscillations were abolished when actomyosin was disabled by perturbing F-actin, inhibiting ROCK (Rho-associated coiled-coil containing protein kinase) (Fig. 3g,h and Supplementary Fig. 3b), or by myosin II RNA-mediated interference (RNAi; Fig. 3i,j and Supplementary Fig. 3c,d and Video 7). Together, these findings indicated that the actomyosin cortex exerts force on lateral cadherin clusters, as it does at the zonula adherens. However, the differences in movement emphasized that contractile outcomes were different in these two intra-junctional regions.

E-cadherin establishes the contractile lateral cortex

Interestingly, oscillatory motion at the lateral membrane was not confined to cadherins, as clusters of caveolin-1–GFP (Cav1–GFP)[36] exhibited similar patterns of movement (Fig. 4a,b and Supplementary

Fig. 4b,c and Videos 4, 8). This was not due to passive movement of both cadherin and caveolin in the lateral membrane, because Cav1–GFP oscillations were substantially reduced by E-cadherin short interfering RNA (siRNA; Fig. 4a,b and Supplementary Fig. 4b,c and Video 4). Instead, this implied that E-cadherin participated in establishing lateral contractility, which was then propagated to other membrane proteins.

One potential mechanism for E-cadherin to support lateral junction contractility lies in its capacity to induce cortical actin assembly through the Arp2/3 actin nucleator[16,37,38]. Indeed, Arp3 often decorated lateral E-cadherin clusters (Fig. 4c,d) and both lateral Arp3 (Fig. 4c,e and Supplementary Fig. 4d), and lateral F-actin (Fig. 4f,g), were substantially reduced by E-cadherin RNAi. Further, lateral F-actin was reduced when the Arp2/3 complex was disrupted with ArpC2 siRNA (Fig. 4h,i and Supplementary Fig. 4f). This implied that cadherin-based Arp2/3 supported the lateral actin network, as it does at the zonula adherens[16]. As F-actin is required for actomyosin self-assembly[39], we then tested directly whether Arp2/3 affected contractile behaviour at the lateral junctions. Indeed, ArpC2 siRNA inhibited the oscillatory
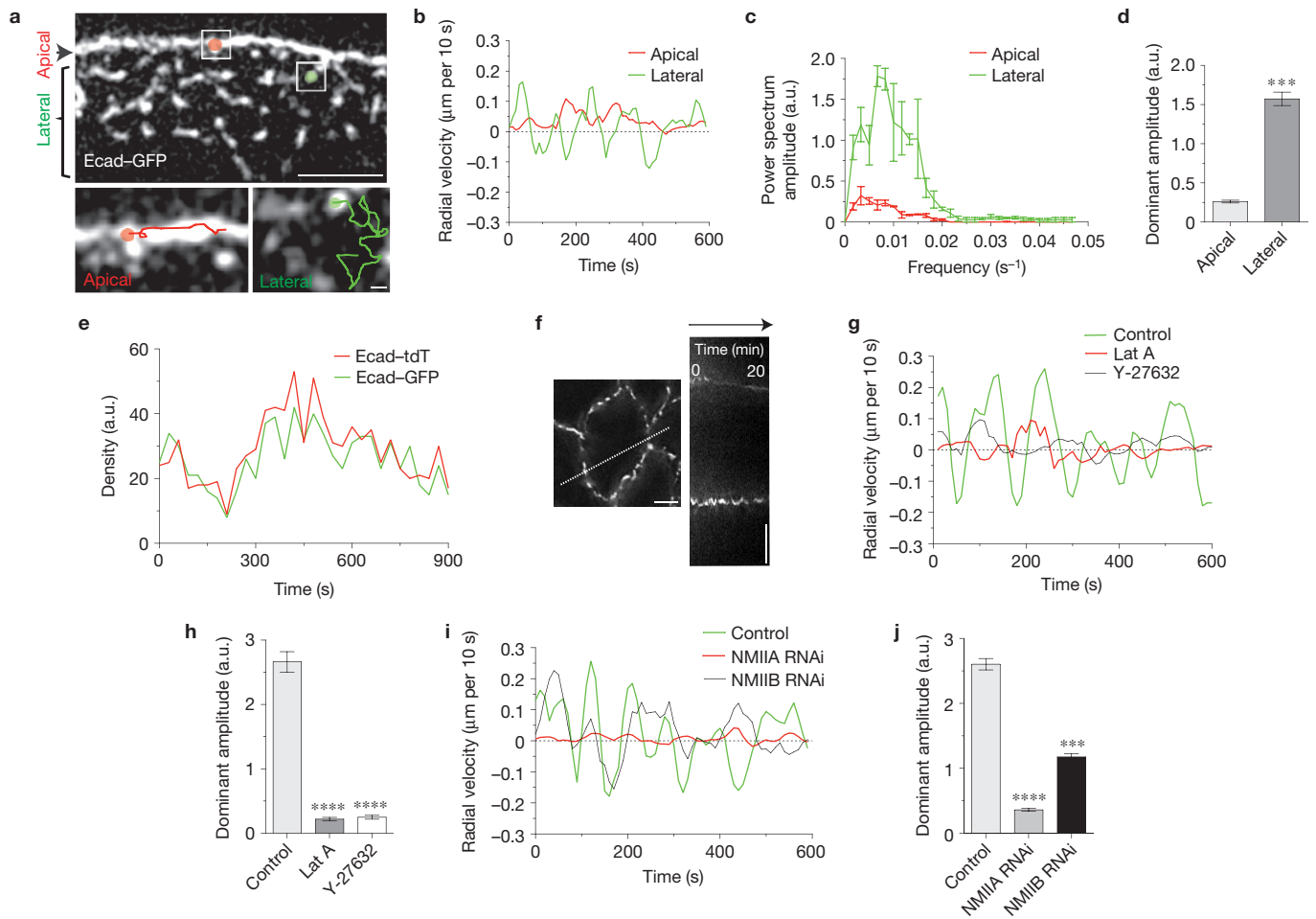
Figure 3 Actomyosin contractility generates different patterns of motion on apical and lateral E-cadherin clusters. (**a**) Ecad–GFP at an *en face* cell–cell contact. Details: magnified views of apical (zonula adherens) and lateral cadherin clusters with superimposed particle tracks. (**b**) Representative radial velocity traces of apical and lateral clusters. (**c, d**) Fourier analysis of E-cadherin radial velocity showing the power spectrum amplitude for the full-range of frequencies (**c**) and the dominant amplitude (**d**) at the principal oscillation frequency. (**e**) Ecad–GFP and Ecad–tdT density fluctuations within a 1 μm² region of analysis at the lateral junctions (Pearson's coefficient: 0.86). (**f**) The lateral junctional domain does not constrict over time. Kymograph of indicated line, of the left image. (**g**,**h**) Representative radial velocity traces of lateral clusters after dimethylsulphoxide (Control), latrunculin A (Lat A, 1 μM) or Y-27632 (30 μM) treatment (**g**) and the corresponding dominant amplitude (**h**). (**i**,**j**) Representative radial velocity traces (**i**) and dominant amplitude (**j**) of lateral cluster movement in control, NMIIA RNAi or non-muscle myosin heavy chain IIB (NMIIB, also known as MYH10) RNAi cells. For **c**,**d**,**h**,**j** data are means ± s.e.m. from $n = 3$ independent experiments, ***$P < 0.001$, ****$P < 0.0001$; with one-way ANOVA, Dunnett's *post hoc* test in **h**,**j** and with Student's *t*-test in **d**. Detailed statistical information and source data are in Supplementary Table 1. All scale bars are 5 μm except for the magnified view of the lateral cluster in **a**, which is 0.5 μm.

motion of lateral cadherin clusters (Fig. 4j,k and Supplementary Fig. 4e and Video 9) and also reduced cortical myosin II itself (Fig. 4l–n and Supplementary Fig. 4f). Together, these findings suggest that actin assembly allows E-cadherin adhesion to establish the contractile lateral cortex by providing the cortical scaffold necessary for myosin incorporation.

Myosin II drives oscillatory fluctuations in the lateral F-actin network

Myosin can exert complex effects on actin networks[40–42] that potentially affect contractility. We therefore used dual-colour Videos to analyse the dynamics of F-actin (Tag-RFP-T–UtrCH; ref. 43) at the lateral junction (identified with Ecad–GFP; Fig. 5a and Supplementary Fig. 5a and Video 10). These demonstrated that the short actin cables seen

by immunofluorescence represented transient structures that typically terminated in, and often bridged between, cadherin clusters (Fig. 5b,c). Closer inspection revealed further that the cables were embedded in a less intense actin network distributed isotropically throughout the lateral cortex (Fig. 5d and Supplementary Video 10). Strikingly, the actin cables seemed to represent transient local intensifications within the isotropic network (mean lifetime ∼ 50 s, Fig. 5d,e), yielding cyclic fluctuations in F-actin fluorescence (Fig. 5f,g). These local intensifications of F-actin resembled the aggregation that occurs when purified actin filaments and myosins are mixed[44]. Indeed, cyclic fluctuations in lateral F-actin intensity were substantially reduced by myosin II RNAi (Fig. 5f,g and Supplementary Video 7).

This supported the notion that F-actin cables represent contractile condensations within an isotropic cortical actin network at the
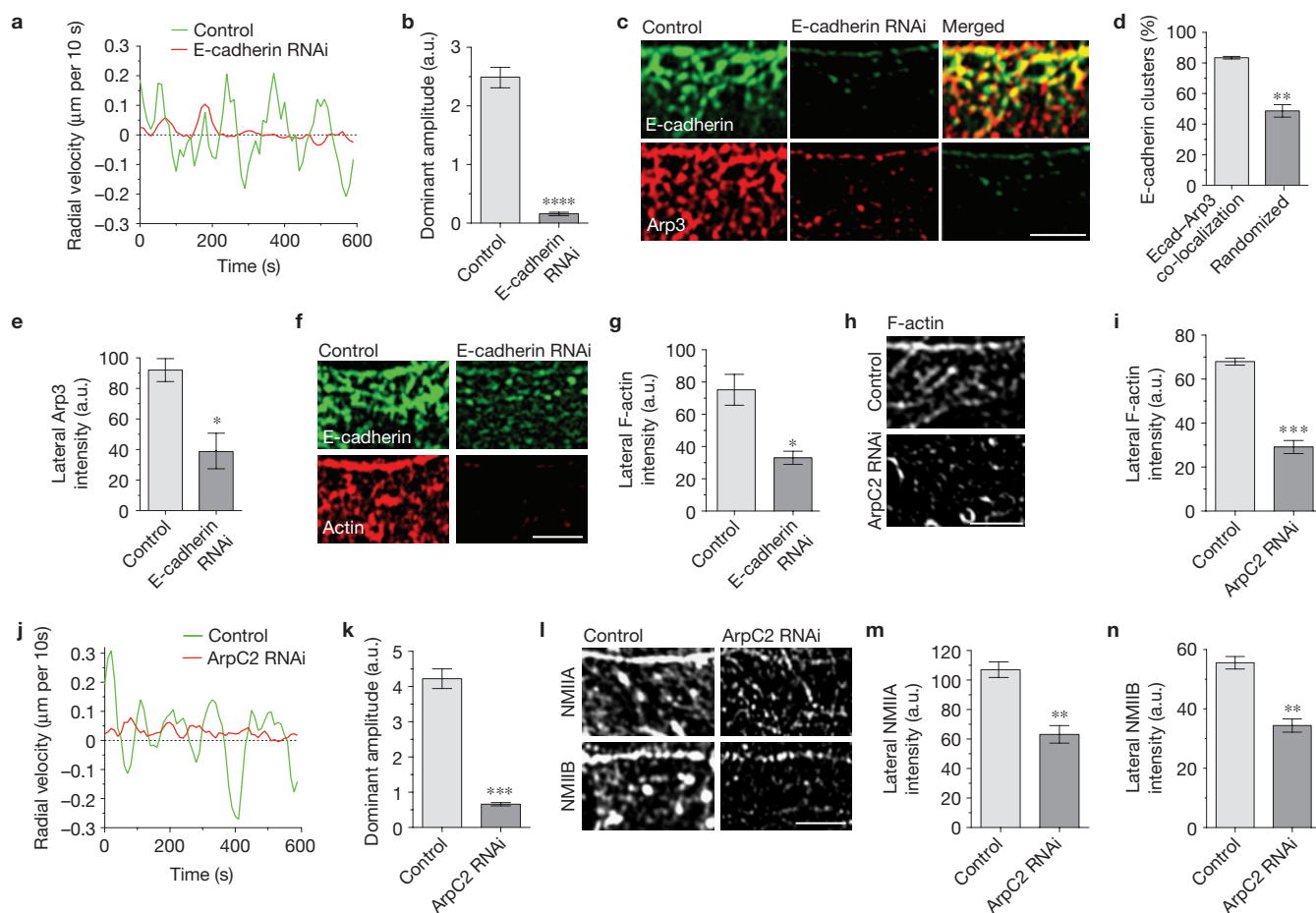
Figure 4 E-cadherin establishes the contractile lateral cortex through actin assembly. (**a**,**b**) Representative radial velocity traces (**a**) and dominant amplitude (**b**) of Cav1–GFP at lateral junctions in control and E-cadherin RNAi cells. (**c**–**e**) E-cadherin supports lateral Arp2/3. (**c**) Representative images of E-cadherin and Arp3 in control and E-cadherin RNAi cells. (**d**) Co-localization of E-cadherin and Arp3 quantified at the lateral junctions of control cells and compared with randomized Ecad/Arp3 image Z-stacks of the same regions. (**e**) Lateral Arp3 fluorescence intensity in control and E-cadherin RNAi cells. (**f**,**g**) Representative images (**f**) of junctional lateral junctions[44]. By analogy with *in vitro* models of actomyosin condensation, local stresses exerted by motors may cause actin filaments to buckle[44,45] and reorganize, thereby promoting contractility and cable formation. Sustained contractility, however, can also induce F-actin disassembly[42,45,46]. Indeed, photoactivated PA-GFP–actin decayed more slowly (Fig. 5h,i), and actin cable lifetime was increased (Fig. 5e), at the lateral junctions in myosin IIA knockdown (RNAi) cells. Thus, the cyclical pattern of F-actin condensation and dissipation seen at the lateral junctions reflects the action of myosin II to initially aggregate cortical actin filaments, and then disassemble the condensed F-actin (Supplementary Fig. 5b).

Cortical F-actin condensation also typically coincided with congression of associated cadherin clusters (Fig. 5d,j and Supplementary Fig. 5a), whereas F-actin cables dissipated when clusters separated. This suggested that actin filament disassembly also contributed to oscillatory motion, presumably by facilitating separation of clusters. Indeed, stabilization of F-actin with jasplakinolide reduced cadherin

E-cadherin (green) and F-actin (red) in either control or E-cadherin RNAi cells and corresponding lateral F-actin fluorescence intensity quantification (**g**). (**h**–**n**) Effect of ArpC2 RNAi on lateral F-actin fluorescence intensity (**h**,**i**), radial velocity traces (**j**) and dominant amplitude analysis (**k**) of lateral cluster oscillations, and on lateral NMIIA (**l**,**m**) and NMIIB (**l**,**n**) localization and fluorescence intensity. All data are means ± s.e.m. from $n = 3$ independent experiments, $*P < 0.05$, $**P < 0.01$, $***P < 0.001$, $****P < 0.0001$; analysed with Student's t-test (statistical information and source data in Supplementary Table 1). Scale bars, 5 μm.

oscillations (Fig. 5k and Supplementary Fig. 5c,d and Video 11). Thus, the oscillatory motion of lateral cadherin clusters reflects the biphasic impact of myosin II, to condense, and then turn over, local cortical actin networks (Fig. 5l).

Local actin stabilization by N-WASP determines the apico-lateral pattern of junctional tension

As rapid local F-actin turnover characterized the lateral cortex, we then investigated how it compared with that at the zonula adherens. Strikingly, F-actin seemed significantly more stable at the zonula adherens than at the lateral junctions (Fig. 6a,a' and Supplementary Video 12) and photoactivated PA-GFP–actin decayed more slowly there than at the lateral junctions (Fig. 6b,b'). This suggested the hypothesis that differential stabilization of F-actin might be responsible for the differences in tension seen at these two zones.

To pursue this, we sought to identify a regulator of actin stability that promoted tension at the zonula adherens. One such candidate
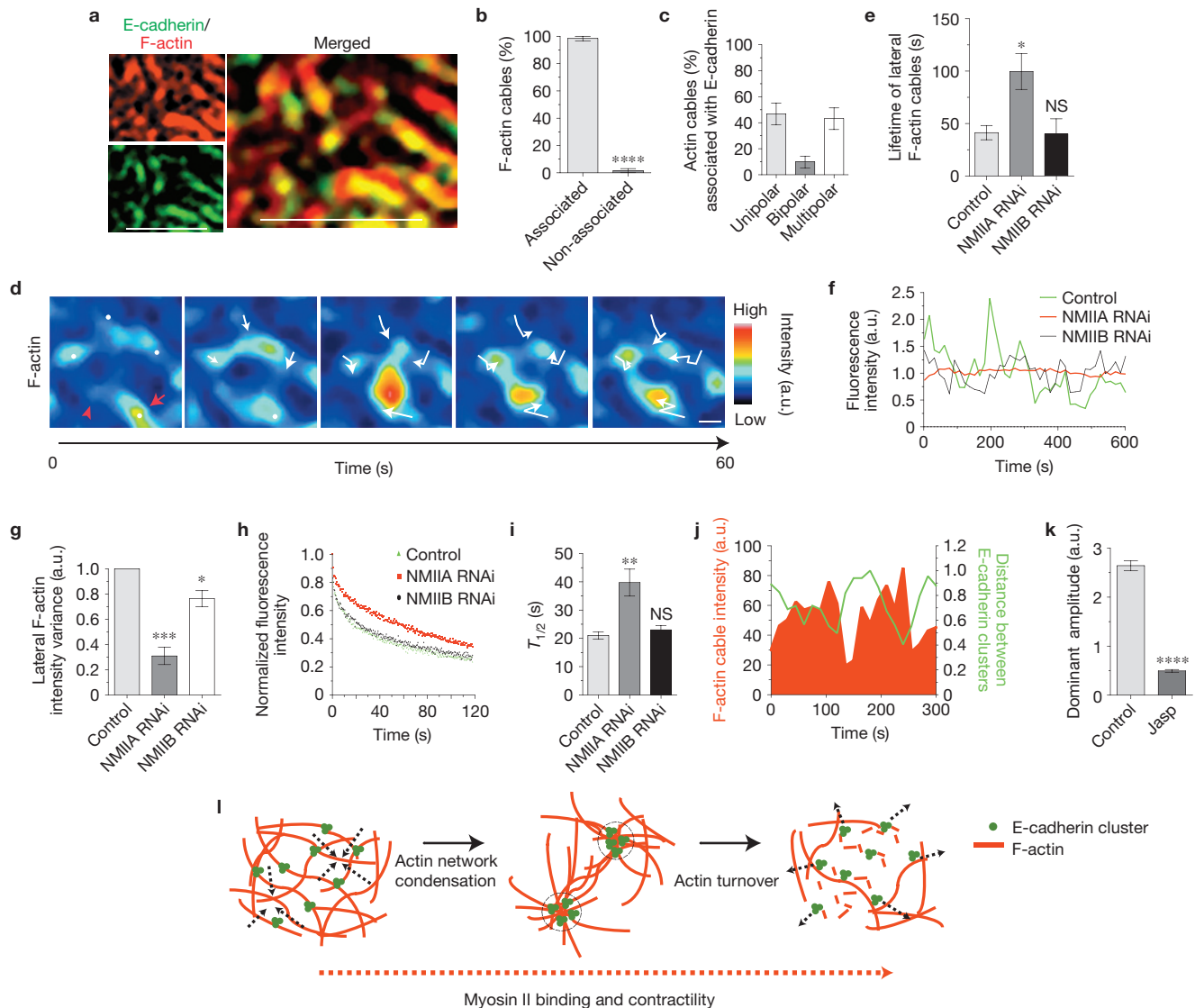
Figure 5 Myosin II drives oscillatory fluctuations in the lateral F-actin network. (**a**) Representative still image of lateral Ecad–GFP and F-actin (Tag-RFP-T–UtrCH). (**b**) Percentage of F-actin cables either associated or not associated with E-cadherin clusters. Data are means ± s.e.m. from $n = 4$ independent experiments. (**c**) Percentage of actin cables that associate with an E-cadherin cluster at one end (unipolar); actin cables that bridged two clusters (bipolar); and actin cables where multiple cables form a series of bridges between clusters (multipolar). (**d**) Time series of F-actin condensation (red arrow) within an isotropic cortical network (red arrowhead) with superimposed tracks (white arrows) of cadherin clusters. (**e**) Lateral F-actin cable lifetime in control NMIIA RNAi and NMIIB RNAi cells. (**f**,**g**) Representative temporal changes in lateral F-actin intensity (**f**) and intensity variance (**g**) in control, NMIIA RNAi and NMIIB RNAi cells.

(**h**,**i**) Fluorescence decay after photoactivation of mRFP–PA-GFP–actin at lateral junctions: normalized fluorescence intensity decay (**h**) and half-life (**i**) in control, NMIIA RNAi and NMIIB RNAi cells. (**j**) Representative temporal changes in F-actin cable intensity and distance between E-cadherin clusters. (**k**) Dominant amplitude derived from Fourier analysis of lateral E-cadherin cluster oscillations in cells treated with either dimethylsulphoxide (Control) or jasplakinolide (Jasp, 0.2 μM). (**l**) Cartoon of actomyosin-driven E-cadherin cluster oscillations. Arrows indicate direction of E-cadherin cluster movements. All data are means ± s.e.m. calculated from $n = 3$ independent experiments; NS, not significant; *$P < 0.05$, **$P < 0.01$, ***$P < 0.001$, ****$P < 0.0001$; all analyses are with one-way ANOVA, Dunnett's *post hoc* test except **b** and **k**, which were with Student's *t*-test (statistical information and source data in Supplementary Table 1). Scale bars, 5 μm (**a**), 0.5 μm (**d**).

was N-WASP (ref. 47), which concentrates at the zonula adherens (Fig. 6c,c',d,d')[48], where it stabilizes actin filaments through association with the WIP family protein[49], WIRE (ref. 28). Indeed, N-WASP RNAi effectively abolished the differences in zonula adherens and lateral tension, specifically reducing apical junction tension to levels similar to the lateral junctions of control cells (Fig. 6e and Supplementary Fig. 6a). We earlier demonstrated that N-WASP RNAi fragmented the zonula adherens into apical clusters, without altering epithelial polarity[28]. Live

imaging now revealed that these apical clusters exhibited a tenfold increased oscillatory motion (Fig. 6f and Supplementary Fig. 6b,b',c and Video 13), providing further evidence that the distinctive contractile properties of the zonula adherens were determined by N-WASP.

We then investigated whether ectopic targeting of N-WASP could stabilize F-actin to alter contractile behaviour at the lateral junctions. As the VCA domain can autoinhibit N-WASP (ref. 47) and is dispensable for N-WASP to stabilize F-actin at adherens
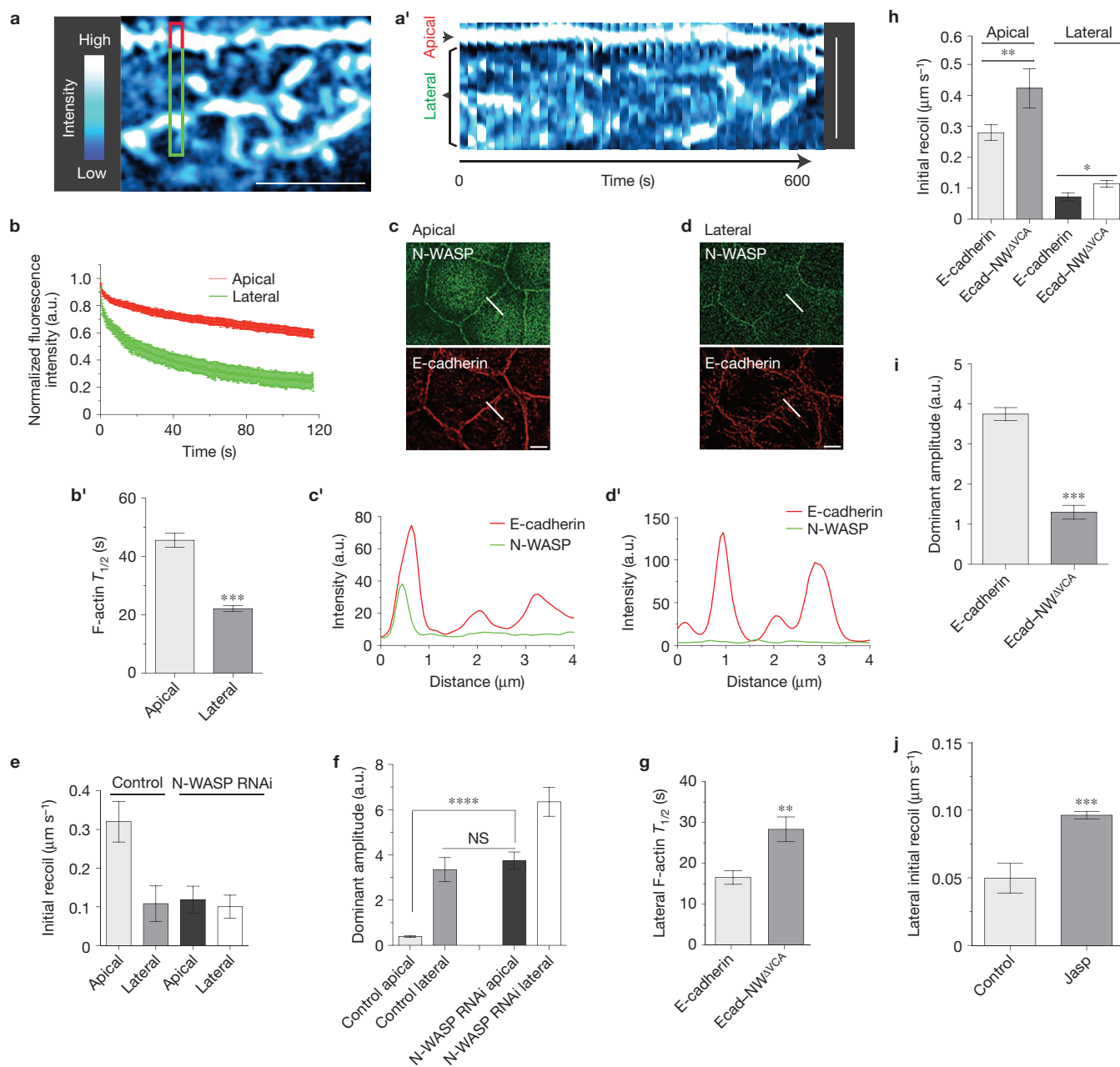
Figure 6 Local F-actin stabilization by N-WASP determines the apical–lateral pattern of junctional contractility. (**a**) Representative still image from a junctional F-actin (GFP–UtrCH) time-lapse series (colour encoded with hot cyan) and the corresponding heat map (left). (**a'**) Kymograph of indicated area on **a**. (**b**) Average decay curves (**b**) and half-lives (**b'**) of lateral PA-GFP–actin fluorescence intensity after photoactivation. (**c,d**) Representative images (**c,d**) and fluorescence line-scan analysis (**c',d'**) of E-cadherin and N-WASP at either the apical (**c,c'**) or lateral (**d,d'**) junctions. (**e**) Tension data for apical and lateral junctions in control and N-WASP RNAi cells. (**f**) Dominant amplitude from the Fourier analysis of zonula adherens and lateral E-cadherin radial velocity in control and N-WASP RNAi cells. (**g**) Lateral F-actin half-life of E-cadherin RNAi cells reconstituted with Ecad–GFP or Ecad–GFP–N-WASP$^{\Delta VCA}$. (**h**) Apical

and lateral junction tension in E-cadherin RNAi cells reconstituted with Ecad–GFP or Ecad–GFP–N-WASP$^{\Delta VCA}$. (**i**) Dominant amplitude from the Fourier analysis of lateral Ecad–GFP and Ecad–GFP–N-WASP$^{\Delta VCA}$ radial velocity in E-cadherin RNAi cells. (**j**) Lateral tension in dimethylsulphoxide (Control) or jasplakinolide (Jasp)-treated cells. All data are means ± s.e.m.; NS, not significant; *$P < 0.05$, **$P < 0.01$, ***$P < 0.001$, ****$P < 0.0001$; calculated from $n = 3$ independent experiments except for **e**, which were technical replicates (means ± s.d., $n = 19$) of one representative experiment from two independent repeats. All data were analysed with nonlinear regression analysis except **b',i,g**, which were with Student's t-test, and **f**, which was with one-way ANOVA, Dunnett's post hoc test (statistical information and source data in Supplementary Table 1). Scale bars, 5 µm.

junctions[28], we fused N-WASP lacking the VCA (N-WASP$^{\Delta VCA}$) to E-cadherin (Ecad–N-WASP$^{\Delta VCA}$, Supplementary Fig. 6d,e) and expressed this in E-cadherin RNAi cells, where it distributed, with WIRE,

throughout the junctions (Supplementary Fig. 6f) and stabilized lateral F-actin (Fig. 6g). Consistent with our hypothesis, lateral tension was increased, and oscillatory motion decreased, in Ecad–N-WASP$^{\Delta VCA}$
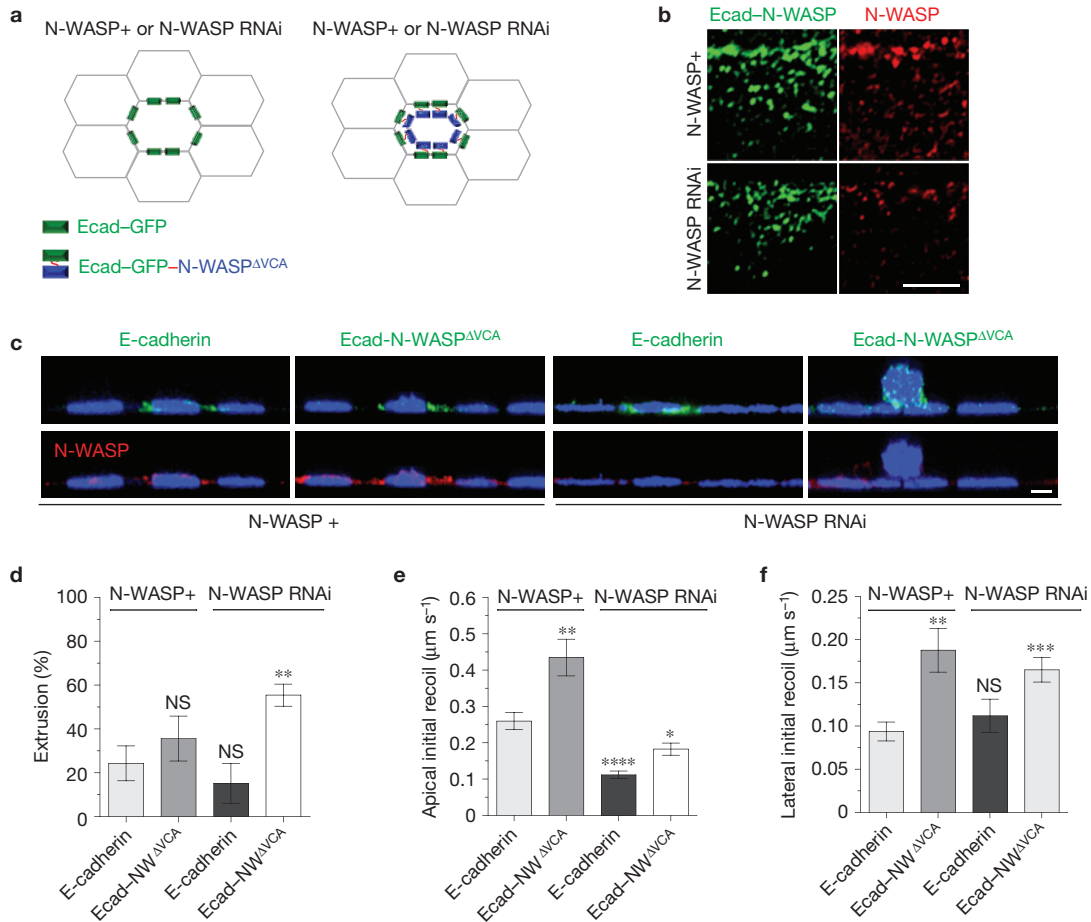
Figure 7 Redistributing N-WASP into the lateral cortex drives apical extrusion. (**a**) Experimental design of Ecad–GFP or Ecad–GFP–N-WASP$^{\Delta VCA}$ expressed mosaically within either N-WASP + or N-WASP RNAi monolayers. (**b**) Representative images of junctional Ecad–N-WASP$^{\Delta VCA}$ and endogenous N-WASP at the interface of heterologous contacts within N-WASP RNAi and N-WASP + monolayers. (**c**,**d**) Representative *XZ* images (**c**) and quantification (**d**) of either single Ecad–GFP or Ecad–GFP–N-WASP$^{\Delta VCA}$-expressing cells undergoing extrusion from epithelial sheets in N-WASP+ or N-WASP RNAi monolayers. (**e**,**f**) Apical (**e**) and lateral (**f**) tension at heterologous junctions between individual cells expressing either Ecad–GFP or Ecad–GFP–N-WASP$^{\Delta VCA}$ and neighbour cells in N-WASP + or N-WASP RNAi monolayers. All data are means ± s.e.m.; NS, not significant; *$P < 0.05$, **$P < 0.01$, ***$P < 0.001$, ****$P < 0.0001$; calculated from $n = 3$ independent experiments analysed with nonlinear regression except **d**, which was with one-way ANOVA, Tukey's multiple comparison test (statistical information and source data in Supplementary Table 1). Scale bars, 5 μm.

cells compared with controls (Fig. 6h,i and Supplementary Fig. 7a–c and Video 14). Apical tension was also increased (Fig. 6h), as might be expected as the fusion protein also localized in this region. Independent stabilization of F-actin with jasplakinolide[50] also increased tension at the lateral junctions (Fig. 6j and Supplementary Fig. 7d). Therefore, the cortical distribution of N-WASP can regulate the pattern of junctional contractility through local stabilization of F-actin networks.

Redistributing N-WASP into the lateral cortex drives apical extrusion

We then examined how control of intra-junctional tension might influence epithelial organization. We first assessed the consequences of redistributing N-WASP activity from the zonula adherens into the lateral junctions. To that end, we expressed Ecad–N-WASP$^{\Delta VCA}$ to generate a lateral pool of active N-WASP and also depleted the endogenous N-WASP pool (Fig. 7a), which otherwise continues to accumulate with Ecad–N-WASP$^{\Delta VCA}$ at apical junctions (Fig. 7b).

Strikingly, we found that expressing Ecad–N-WASP$^{\Delta VCA}$ in single cells within N-WASP-depleted monolayers promoted apical extrusion of these cells (Fig. 7c,d). This did not occur when Ecad–N-WASP$^{\Delta VCA}$ was mosaically expressed in N-WASP-containing (N-WASP+) cells (Fig. 7c,d) nor when Ecad–GFP was expressed mosaically under any circumstances (Fig. 7c,d).

We then characterized the patterns of intra-junctional tension at the heterologous contacts formed between transgene-expressing cells and their neighbours when either Ecad–GFP or Ecad–N-WASP$^{\Delta VCA}$ was expressed mosaically within N-WASP+ or N-WASP RNAi monolayers. Compared with Ecad–GFP controls, both apical and lateral tension were increased at heterologous contacts when Ecad–N-WASP$^{\Delta VCA}$ was expressed in N-WASP+ cells. In contrast, N-WASP RNAi cells expressing Ecad–N-WASP$^{\Delta VCA}$ showed reduced apical tension but persistently elevated lateral tension at heterologous contacts (Fig. 7e,f and Supplementary Fig. 7e,f). This suggested that altered patterns of intra-junctional contractility, driven by mosaic redistribution of N-WASP from apical to lateral junctions, could induce cell extrusion.
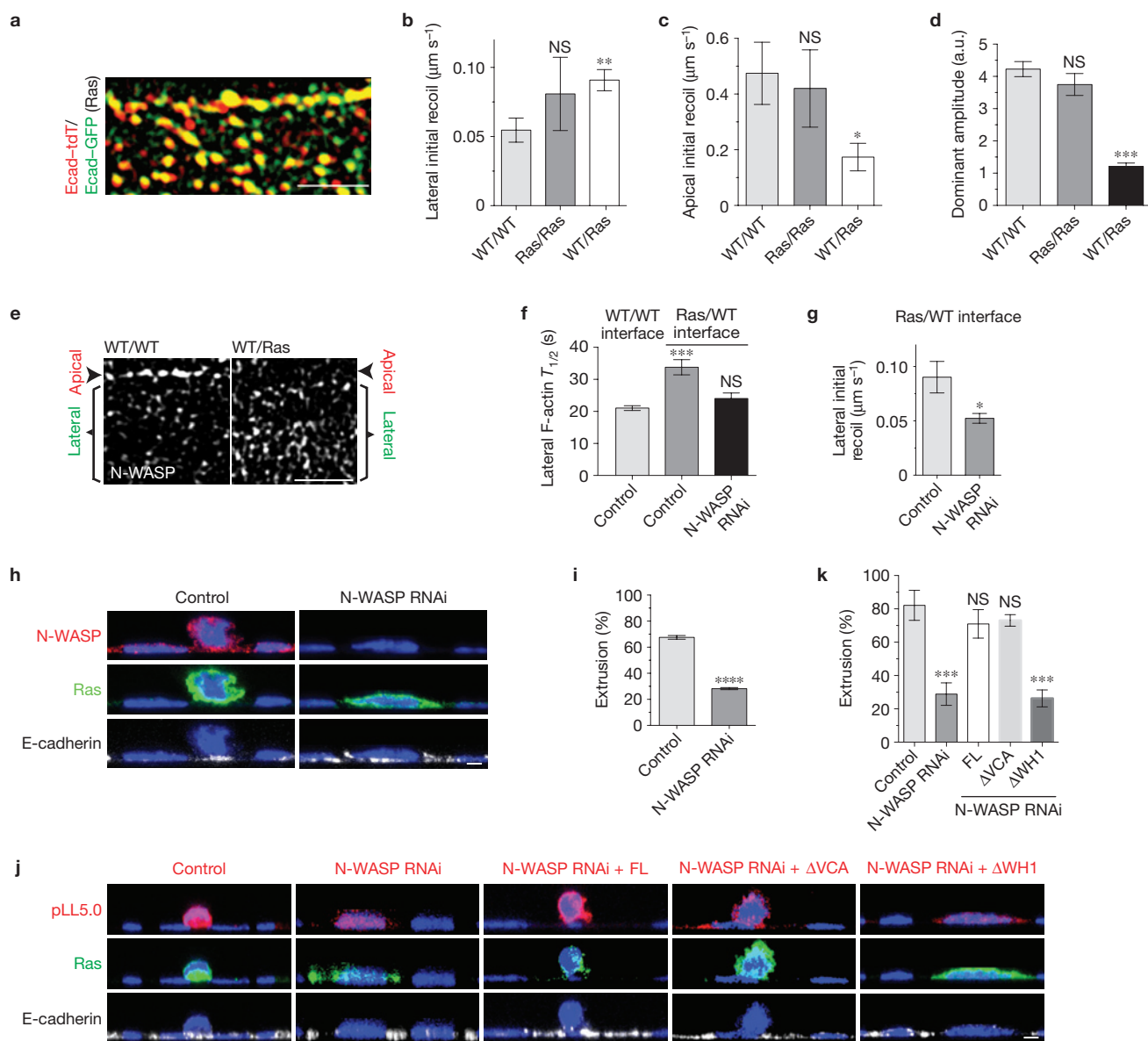
Figure 8 Dysregulated apical–lateral patterns of junctional contractility drive oncogenic extrusion. (**a**) Cadherins assemble homophilic clusters at interfaces between WT (Ecad–tdT) and H-Ras^{V12}-expressing (Ecad–GFP) cells. (**b,c**) Lateral (**b**) and apical (**c**) junctional tension at interfaces between WT/WT, H-Ras^{V12}/ H-Ras^{V12} and H-Ras^{V12}/WT cells. (**d**) Dominant amplitude of lateral E-cadherin oscillations at interfaces between WT/WT, H-Ras^{V12}/H-Ras^{V12} and H-Ras^{V12}/WT cells. (**e**) Cortical distribution of N-WASP at interfaces between WT/WT and H-Ras^{V12}/WT cells. (**f**) Lateral F-actin stability ($T_{1/2}$ of fluorescence decay of photoactivated PA-GFP–actin) at the interfaces between WT/WT and H-Ras^{V12}/WT cells in either control or N-WASP RNAi monolayers. (**g**) Lateral junction tension at interfaces between H-Ras^{V12}/WT cells in either control or N-WASP RNAi monolayers. (**h,i**) Representative *XZ* images (**h**) and quantification (**i**) of single H-Ras^{V12}-expressing cells undergoing extrusion from epithelial sheets in either control (scrambled siRNA) or N-WASP siRNA-transfected monolayers. (**j,k**) Representative *XZ* images (**j**) and quantification (**k**) of extrusion of single H-Ras^{V12}-expressing cells co-transfected with either control plasmid, N-WASP shRNA alone or N-WASP shRNA co-expressing shRNA-resistant full-length N-WASP, N-WASP$^{\Delta VCA}$ or N-WASP$^{\Delta WH1}$. All data are means ± s.e.m. calculated from $n = 3$ independent experiments, NS, not significant; *$P < 0.05$, **$P < 0.01$, ***$P < 0.001$, ****$P < 0.0001$; **b,c,g** were analysed with nonlinear regression analysis, **d,f,k** with one-way ANOVA, Dunnett's *post hoc* test, and **i** with Student's *t*-test (statistical information and source data in Supplementary Table 1). Scale bars, 5 μm.

Dysregulated apical–lateral patterns of junctional contractility drive oncogenic extrusion

Finally, we investigated whether patterns of intra-junctional tension were altered in an established model of cell extrusion, when minorities of H-Ras^{V12}-expressing cells are surrounded by wild-type (WT) neighbours (Fig. 8h,j)[13]. In these mosaic cultures, E-cadherin still formed homophilic clusters at the interfaces between WT and H-Ras^{V12}-expressing cells (Fig. 8a and Supplementary Fig. 8a,b and Video 15). However, even before overt extrusion had occurred, lateral tension was increased, accompanied by decreased cluster oscillations (Fig. 8b,d and Supplementary Fig. 8d–f), whereas apical tension was reduced towards that in the lateral junctions (Fig. 8c and Supplementary Fig. 8c). This resembled exactly the pattern that we saw when we experimentally redistributed N-WASP to the lateral junctions

in cells depleted of endogenous N-WASP. Indeed, at the H-Ras^{V12}/WT interface, N-WASP was reduced at the apical junctions and increased at the lateral zones (Fig. 8e), where cortical F-actin stability was also increased (Fig. 8f). Further, both the increased lateral tension (Fig. 8g and Supplementary Fig. 8g) and F-actin stabilization (Fig. 8f) seen at the WT/H-Ras^{V12} junctions were abolished by N-WASP RNAi, supporting the notion that redistribution of N-WASP was responsible for the altered pattern of intra-junctional tension.

Importantly, extrusion was significantly reduced when N-WASP was depleted by RNAi (Fig. 8h–k). This occurred when N-WASP was reduced throughout the monolayer by siRNA (Fig. 8h,i) and also when it was reduced specifically in the oncogene-expressing cell by co-expression of N-WASP short hairpin RNA (shRNA; Fig. 8j,k). Extrusion was restored when RNAi-resistant N-WASP was reconstituted in the H-Ras^{V12}-expressing cells (Fig. 8j,k). Therefore, N-WASP was required in the oncogene-transfected cells for extrusion to occur. Further, the molecular requirement mapped to the WH1 domain of N-WASP that is responsible for junctional F-actin stabilization[28]. Extrusion was restored when shRNA-transfected cells were reconstituted with RNAi-resistant N-WASP$^{\Delta VCA}$, but not with a mutant that lacks the WH1 domain (Fig. 8j,k). Together, these indicate that stringent control of the pattern of intra-junctional tension can determine whether, or not, cells integrate into epithelial monolayers.

DISCUSSION

We have recently come to appreciate how planar patterns of contractile tension affect tissue architecture[51,52]. Junctional tension, the product of integrating adhesion and the contractile cortex, has often been treated as principally a property of the apical junctions[1,53] or as a homogeneous feature of cell–cell contacts[2]. Our present findings show, however, that contractility is also regulated to establish apical–lateral patterns of junctional tension that can determine whether, or not, cells integrate into epithelia.

We propose that E-cadherin adhesion serves a central role in establishing the contractile cortex at cell–cell contacts. This is mediated by cadherin-based assembly of the cortical actin cytoskeleton, which can promote the incorporation of activated myosin through self-assembly[54]. This process occurs both at the zonula adherens (ref. 16) and lateral junctions. However, the contractile outcome also depends on how local actin networks respond to contractility[55]. The distinctive oscillatory motion of cadherin clusters that we have identified in the lateral junctions seems to reflect a biphasic impact of myosin contractility on cortical actin: initial condensation that drives congression of clusters and then stress-induced filament turnover that facilitates their separation. These coupled phases imply that this system contains an intrinsic capacity to limit its contractile output, as filament turnover will disable the capacity of actomyosin to generate tension. Consistent with this, lateral tension was increased when F-actin was stabilized with jasplakinolide. The limited capacity to generate contractility is further supported by the observation that oscillations did not lead to net constriction of the lateral junctions. What defines the distinctive kinetic properties of this oscillatory system remains to be elucidated, but for our present consideration, oscillations can be regarded as identifying this self-limited mode of junctional contractility.

Self-limited contractility can be overcome by local stabilization of the actin networks that interact with myosin. Our present experiments identify a key role for N-WASP, which we earlier found to stabilize F-actin nucleated at the zonula adherens[28]. Depletion of N-WASP reduced apical tension to levels comparable to those at the lateral junction; it also caused apical cadherin clusters to exhibit oscillatory motion, consistent with the notion that contractility had become self-limited. Effectively, the contractile properties of the apical junctional cortex became indistinguishable from those of the lateral junctions when N-WASP was depleted. It should be emphasized that we do not exclude the capacity of other factors (for example, myosin regulation itself) to modulate contractility. Nonetheless, the capacity of the Ecad–N-WASP$^{\Delta VCA}$ fusion protein to increase lateral tension indicates that local changes in N-WASP activity can modulate contractile outcomes in a manner independent of other regulatory factors. In this scheme, the self-limited contractility shown by the lateral junctions might be thought of as the basic contractile system, which is then tuned by local stabilization of actin. One potential design advantage of this system is that it would allow contractility and tension to be locally modulated through a pathway that is orthogonal to the signalling pathways that regulate myosin II activity.

One possible mechanism for N-WASP to stabilize F-actin lies in modulation of filament organization[41]. As F-actin at the lateral cortex requires Arp2/3, it is likely to be initially generated as branched networks that may be sensitive to stress-induced filament severing[41]. At the zonula adherens, actin is also nucleated by Arp2/3 but eventually incorporates into perijunctional bundles[16,28], where filaments are likely to be co-aligned with myosin. An extreme form of this co-alignment is the sarcomeric-like organization of actomyosin that has been seen at some adherens junctions[56]. Such alignment may help actin filaments resist contractile stresses[41]. Indeed, N-WASP in cooperation with WIRE is necessary for nascent junctional F-actin to form bundles[28], implying that it contributes to filament reorganization.

We further found that apical–lateral patterning of contractility plays a key role in determining whether or not cells integrate into monolayers. Apical cell extrusion occurred when apical–lateral patterns of contractility were disrupted, either when N-WASP was redistributed during oncogenic extrusion or when it was retargeted experimentally from the apical to lateral junctions. For H-Ras^{V12}-transfected cells, N-WASP was necessary for extrusion to occur, as extrusion was blocked by N-WASP depletion. Although other changes (for example, altered polarity) may occur in the H-Ras^{V12} model, the demonstration that experimental relocalization of N-WASP also caused extrusion implies that the junctional distribution of N-WASP may be an independent determinant of extrusion. Consistent with the mechanism that we have now identified for N-WASP to regulate junctional contractility, lateral F-actin was stabilized at the heterologous contacts. Further, the WH1 domain of N-WASP, which stabilizes F-actin by associating with WIRE (ref. 28), was necessary for extrusion to occur.

Of note, though, increased lateral contractility alone was not sufficient to drive extrusion. Apical tension was also reduced during oncogenic extrusion, accompanied by loss of apical N-WASP. It was also necessary for endogenous N-WASP to be depleted in cells expressing Ecad–N-WASP$^{\Delta VCA}$ for extrusion to occur, a manoeuvre that reduced apical tension in this experimental model. Therefore, extrusion requires an increase in lateral contractility accompanied by decreased apical tension. Together, these observations indicate that

altering the pattern of intra-junctional contractility can perturb the ability of cells to remain integrated within an epithelium.

It is noteworthy that in both experimental systems studied, it was sufficient for N-WASP to be redistributed within a single cell for extrusion to occur. This is consistent with other models where extrusion occurs specifically at heterologous cell–cell interfaces formed between minorities of apoptotic[11,12,57,58] or oncogene-transfected cells[13,59,60] that are surrounded by normal cells. Similar heterologous contacts, where N-WASP was redistributed in a single cell or small groups of cells, were a defining feature in our experiments. Further studies will be necessary to determine how altered apical–lateral patterns of junctional tension lead to cells being extruded. One possibility is that high apical tension serves as an anchor to retain cells within a monolayer, which is lost when the apical tension generator is compromised. This may not be consequential unless accompanied by increased lateral tension, tending to constrict those regions of the cell. Whether lateral tension is increased solely through contractility in the cell to be extruded, or whether it also reflects contractile responses in the neighbouring cells[11–13,57] remains to be determined.

Although our present experiments focused on cell integration, we anticipate that local regulation of junctional contractility by actin stabilization may participate in other morphogenetic events where patterns of tension are regulated to modulate cell-on-cell movements. Answering these questions will be a clear priority for future research.□

METHODS

Methods and any associated references are available in the online version of the paper.

Note: Supplementary Information is available in the online version of the paper

AUTHOR CONTRIBUTIONS
S.K.W., G.A.G., Z.N. and A.S.Y. conceived the project; S.K.W. performed most of the experiments except for the nanoablation and western analyses, which were shared with G.A.G., M.M. and S.V.; R.G.P. contributed to caveolin analysis; S.K.W., G.A.G., J.G.L. and H.L.C. quantified the data; S.K.W., G.A.G., N.A.H. and Z.N. performed quantitative modelling; S.K.W., G.A.G. and A.S.Y. analysed the data and wrote the paper.

1. Sawyer, J. M. *et al.* Apical constriction: a cell shape change that can drive morphogenesis. *Dev. Biol.* **341**, 5–19 (2010).
2. Maitre, J. L. *et al.* Adhesion functions in cell sorting by mechanically coupling the cortices of adhering cells. *Science* **338**, 253–256 (2012).
3. Liu, Z. *et al.* Mechanical tugging force regulates the size of cell–cell junctions. *Proc. Natl Acad. Sci. USA* **107**, 9944–9949 (2010).
4. Maruthamuthu, V., Sabass, B., Schwarz, U. S. & Gardel, M. L. Cell-ECM traction force modulates endogenous tension at cell–cell contacts. *Proc. Natl Acad. Sci. USA* **108**, 4708–4713 (2011).
5. le Duc, Q. *et al.* Vinculin potentiates E-cadherin mechanosensing and is recruited to actin-anchored sites within adherens junctions in a myosin II-dependent manner. *J. Cell Biol.* **189**, 1107–1115 (2010).
6. Borghi, N. *et al.* E-cadherin is under constitutive actomyosin-generated tension that is increased at cell–cell contacts upon externally applied stretch. *Proc. Natl Acad. Sci. USA* **109**, 12568–12573 (2012).
7. Ratheesh, A. *et al.* Centralspindlin and alpha-catenin regulate Rho signalling at the epithelial zonula adherens. *Nat. Cell Biol.* **14**, 818–828 (2012).
8. Fernandez-Gonzalez, R., Simoes Sde, M., Roper, J. C., Eaton, S. & Zallen, J. A. Myosin II dynamics are regulated by tension in intercalating cells. *Dev. Cell* **17**, 736–743 (2009).
9. Monier, B., Pelissier-Monier, A., Brand, A. H. & Sanson, B. An actomyosin-based barrier inhibits cell mixing at compartmental boundaries in *Drosophila* embryos. *Nat. Cell Biol.* **12**, 60–65 (2009).
10. Wu, S. K. & Yap, A. S. Patterns in space: Coordinating adhesion and actomyosin contractility at E-cadherin junctions. *Cell Commun. Adhes.* **20**, 201–212 (2013).
11. Rosenblatt, J., Raff, M. C. & Cramer, L. P. An epithelial cell destined for apoptosis signals its neighbors to extrude it by an actin- and myosin-dependent mechanism. *Curr. Biol.* **11**, 1847–1857 (2001).
12. Slattum, G., McGee, K. M. & Rosenblatt, J. P115 RhoGEF and microtubules decide the direction apoptotic cells extrude from an epithelium. *J. Cell Biol.* **186**, 693–702 (2009).
13. Hogan, C. *et al.* Characterization of the interface between normal and transformed epithelial cells. *Nat. Cell Biol.* **11**, 460–467 (2009).
14. Yonemura, S., Wada, Y., Watanabe, T., Nagafuchi, A. & Shibata, M. alpha-Catenin as a tension transducer that induces adherens junction development. *Nat. Cell Biol.* **12**, 533–542 (2010).
15. Smutny, M. *et al.* Myosin II isoforms identify distinct functional modules that support integrity of the epithelial zonula adherens. *Nat. Cell Biol.* **12**, 696–702 (2010).
16. Verma, S. *et al.* A WAVE2-Arp2/3 actin nucleator apparatus supports junctional tension at the epithelial zonula adherens. *Mol. Biol. Cell* **23**, 4601–4610 (2012).
17. Kraemer, A., Goodwin, M., Verma, S., Yap, A. S. & Ali, R. G. Rac is a dominant regulator of cadherin-directed actin assembly that is activated by adhesive ligation independently of Tiam1. *Am. J. Physiol.* **292**, C1061–C1069 (2007).
18. McLachlan, R. W. & Yap, A. S. Protein tyrosine phosphatase activity is necessary for E-cadherin-activated Src signaling. *Cytoskeleton* **68**, 32–43 (2011).
19. Meng, W., Mushika, Y., Ichii, T. & Takeichi, M. Anchorage of microtubule minus ends to adherens junctions regulates epithelial cell–cell contacts. *Cell* **135**, 948–959 (2008).
20. Larsson, L. I. Distribution of E-cadherin and beta-catenin in relation to cell maturation and cell extrusion in rat and mouse small intestines. *Histochem. Cell Biol.* **126**, 575–582 (2006).
21. Kametani, Y. & Takeichi, M. Basal-to-apical cadherin flow at cell junctions. *Nat. Cell Biol.* **9**, 92–98 (2007).
22. Vaezi, A., Bauer, C., Vasioukhin, V. & Fuchs, E. Actin cable dynamics and Rho/Rock orchestrate a polarized cytoskeletal architecture in the early steps of assembling a stratified epithelium. *Dev. Cell* **3**, 367–381 (2002).
23. Hong, S., Troyanovsky, R. B. & Troyanovsky, S. M. Cadherin exits the junction by switching its adhesive bond. *J. Cell Biol.* **192**, 1073–1083 (2011).
24. Taguchi, K., Ishiuchi, T. & Takeichi, M. Mechanosensitive EPLIN-dependent remodeling of adherens junctions regulates epithelial reshaping. *J. Cell Biol.* **194**, 643–656 (2011).
25. Truong Quang, B. A., Mani, M., Markova, O., Lecuit, T. & Lenne, P. F. Principles of E-cadherin supramolecular organization *in vivo. Curr. Biol.* **23**, 2197–2207 (2013).
26. Gomez, G. A., McLachlan, R. W. & Yap, A. S. Productive tension: force-sensing and homeostasis of cell–cell junctions. *Trends Cell Biol.* **21**, 499–505 (2011).
27. Otani, T., Ichii, T., Aono, S. & Takeichi, M. Cdc42 GEF Tuba regulates the junctional configuration of simple epithelial cells. *J. Cell Biol.* **175**, 135–146 (2006).
28. Kovacs, E. M. *et al.* N-WASP regulates the epithelial junctional actin cytoskeleton through a non-canonical post-nucleation pathway. *Nat. Cell Biol.* **13**, 934–943 (2011).
29. Mangold, S. *et al.* Hepatocyte growth factor acutely perturbs actin filament anchorage at the epithelial zonula adherens. *Curr. Biol.* **21**, 503–507 (2011).
30. Konig, K. Multiphoton microscopy in life sciences. *J. Microsc.* **200**, 83–104 (2000).
31. Woodcroft, B. J., Hammond, L., Stow, J. L. & Hamilton, N. A. Automated organelle-based colocalization in whole-cell imaging. *Cytometry A* **75**, 941–950 (2009).
32. Roh-Johnson, M. *et al.* Triggering a cell shape change by exploiting preexisting actomyosin contractions. *Science* **335**, 1232–1235 (2012).
33. Sako, Y., Nagafuchi, A., Tsukita, S., Takeichi, M. & Kusumi, A. Cytoplasmic regulation of the movement of E-cadherin on the free cell surface as studied by optical tweezers and single particle tracking: corralling and tethering by the membrane skeleton. *J. Cell Biol.* **140**, 1227–1240 (1998).
34. Meijering, E., Dzyubachyk, O. & Smal, I. Methods for cell and particle tracking. *Methods Enzymol.* **504**, 183–200 (2012).

35. Smutny, M. *et al*. Multicomponent analysis of junctional movements regulated by myosin II isoforms at the epithelial zonula adherens. *PLoS ONE* **6,** e22458 (2011).

36. Thomsen, P., Roepstorff, K., Stahlhut, M. & van Deurs, B. Caveolae are highly immobile plasma membrane microdomains, which are not involved in constitutive endocytic trafficking. *Mol. Biol. Cell* **13,** 238–250 (2002).

37. Kovacs, E. M., Goodwin, M., Ali, R. G., Paterson, A. D. & Yap, A. S. Cadherin-directed actin assembly: E-cadherin physically associates with the Arp2/3 complex to direct actin assembly in nascent adhesive contacts. *Curr. Biol.* **12,** 379–382 (2002).

38. Tang, V. W. & Brieher, W. M. alpha-Actinin-4/FSGS1 is required for Arp2/3-dependent actin assembly at the adherens junction. *J. Cell Biol.* **196,** 115–130 (2012).

39. Stachowiak, M. R. *et al*. Self-organization of myosin II in reconstituted actomyosin bundles. *Biophys. J.* **103,** 1265–1274 (2012).

40. Backouche, F., Haviv, L., Groswasser, D. & Bernheim-Groswasser, A. Active gels: dynamics of patterning and self-organization. *Phys. Biol.* **3,** 264–273 (2006).

41. Reymann, A. C. *et al*. Actin network architecture can determine myosin motor activity. *Science* **336,** 1310–1314 (2012).

42. Haviv, L., Gillo, D., Backouche, F. & Bernheim-Groswasser, A. A cytoskeletal demolition worker: myosin II acts as an actin depolymerization agent. *J. Mol. Biol.* **375,** 325–330 (2008).

43. Burkel, B. M., von Dassow, G. & Bement, W. M. Versatile fluorescent probes for actin filaments based on the actin-binding domain of utrophin. *Cell. Motil. Cytoskeleton* **64,** 822–832 (2007).

44. Vogel, S. K., Petrasek, Z., Heinemann, F. & Schwille, P. Myosin motors fragment and compact membrane-bound actin filaments. *eLife* **2,** e00116 (2013).

45. Murrell, M. P. & Gardel, M. L. F-actin buckling coordinates contractility and severing in a biomimetic actomyosin cortex. *Proc. Natl Acad. Sci. USA* **109,** 20820–20825 (2012).

46. Wilson, C. A. *et al*. Myosin II contributes to cell-scale actin network treadmilling through network disassembly. *Nature* **465,** 373–377 (2010).

47. Padrick, S. B. & Rosen, M. K. Physical mechanisms of signal integration by WASP family proteins. *Annu. Rev. Biochem.* **79,** 707–735 (2010).

48. Kovacs, E.M., Verma, S., Thomas, S.G. & Yap, A.S. Tuba and N-WASP function cooperatively to position the central lumen during epithelial cyst morphogenesis. *Cell Adhes. Migrat.* **5,** 344–350 (2011).

49. Martinez-Quiles, N. *et al*. WIP regulates N-WASP-mediated actin polymerization and filopodium formation. *Nat. Cell Biol.* **3,** 484–491 (2001).

50. Cramer, L. P. Role of actin-filament disassembly in lamellipodium protrusion in motile cells revealed using the drug jasplakinolide. *Curr. Biol.* **9,** 1095–1105 (1999).

51. Martin, A. C., Gelbart, M., Fernandez-Gonzalez, R., Kaschube, M. & Wieschaus, E. Integration of contractile forces during tissue invagination. *J. Cell Biol.* **188,** 735–749 (2010).

52. Levayer, R. & Lecuit, T. Oscillation and polarity of E-cadherin asymmetries control actomyosin flow patterns during morphogenesis. *Dev. Cell* **26,** 162–175 (2013).

53. Rauzi, M., Verant, P., Lecuit, T. & Lenne, P. F. Nature and anisotropy of cortical forces orienting *Drosophila* tissue morphogenesis. *Nat. Cell Biol.* **10,** 1401–1410 (2008).

54. Thoresen, T., Lenz, M. & Gardel, M. L. Reconstitution of contractile actomyosin bundles. *Biophys. J.* **100,** 2698–2705 (2011).

55. Bendix, P. M. *et al*. A quantitative analysis of contractility in active cytoskeletal protein networks. *Biophys. J.* **94,** 3126–3136 (2008).

56. Ebrahim, S. *et al*. NMII forms a contractile transcellular sarcomeric network to regulate apical cell junctions and tissue geometry. *Curr. Biol.* **23,** 731–736 (2013).

57. Marshall, T. W., Lloyd, I. E., Delalande, J. M., Nathke, I. & Rosenblatt, J. The tumor suppressor adenomatous polyposis coli controls the direction in which a cell extrudes from an epithelium. *Mol. Biol. Cell* **22,** 3962–3970 (2011).

58. Toyama, Y., Peralta, X. G., Wells, A. R., Kiehart, D. P. & Edwards, G. S. Apoptotic force and tissue dynamics during *Drosophila* embryogenesis. *Science* **321,** 1683–1686 (2008).

59. Leung, C. T. & Brugge, J. S. Outgrowth of single oncogene-expressing cells from suppressive epithelial environments. *Nature* **482,** 410–413 (2012).

60. Kajita, M. *et al*. Interaction with surrounding normal epithelial cells influences signalling pathways and behaviour of Src-transformed cells. *J. Cell Sci.* **123,** 171–180 (2010).

METHODS

Cell culture and transfection. Caco-2 cells were from ATCC (HTB-37) and tested for mycoplasma. In addition, source cultures were maintained in low doses of plasmocin (Invivogen) to prevent mycoplasma contamination. Caco-2 cells were cultured in RPMI media supplemented with 10% FBS, 1% non-essential amino acids, 1% L-glutamine and 1% penicillin/streptomycin. Cells were transfected at 40–60% confluency using Lipofectamine 2000 (Invitrogen) for expression of constructs or RNAi oligonucleotides according to the manufacturer's instructions and analysed 24 h post transfection (at 100% confluency) For live-cell imaging, cells were grown on 29 mm glass-bottomed dishes (Shengyou Biotechnology) and incubated in clear Hank's balanced salt solution supplemented with 5% FBS, 10 mM HEPES at pH 7.4 and 5 mM $CaCl_2$.

For extrusion studies, cells transduced with recombinant lentivirus were mixed with wild-type cells at a 1:5 proportion. The interfaces of cells showing cortical localization of the transgene and wild-type cells were then analysed before extrusion had occurred. Extrusion was quantified in random fields of view as the proportion of transfected cells that were undergoing apical extrusion. To evaluate the frequency of apical oncogenic extrusion, cells were co-transfected at 80% confluency with either $0.2\,\mu g\,ml^{-1}$ of mCherry–H-Ras^{V12} or GFP–H-Ras^{V12} and either pLL5.0 or pLL5.0 N-WASP shRNA or pLL5.0 N-WASP shRNA/N-WASP$^{\Delta VCA}$ or pLL5.0 N-WASP shRNA/N-WASP$^{\Delta WH1}$ or scrambled siRNA or N-WASP siRNA. Single cells co-expressing H-Ras^{V12} with other transgenes surrounded by H-Ras^{V12} null-expressing cells were then analysed at 36 h post transfection. Only cells with an intact nucleus were quantified. For the evaluation of E-cadherin (Ecad)–N-WASP$^{\Delta VCA}$-induced extrusion, we analysed cells with normal cortical localization of the Ecad–N-WASP$^{\Delta VCA}$ or E-cadherin transgenes.

Immunofluorescence and live-cell microscopy. Cells were fixed at $4\,^{\circ}C$ with either $-20\,^{\circ}C$ methanol on ice for 5 min or with 4% paraformaldehyde in cytoskeleton stabilization buffer (10 mM PIPES at pH 6.8, 100 mM KCl, 300 mM sucrose, 2 mM EGTA and 2 mM $MgCl_2$) on ice for 20 min and subsequently permeabilized with 0.2% Triton-X in PBS for 5 min at $4\,^{\circ}C$.

Wide-field images were acquired on a Personal Deltavision deconvolution microscope (Applied Precision) with a Roper Coolsnap HQ2 monochrome camera, and $\times 60$, 1.42 NA, PlanApo objectives or $\times 100$ UPlan SApo, 1.40 NA objectives (Olympus, Japan). Time-lapse and still images were acquired as 10–40 z-stacks (0.1–0.2 μm z-step) and deconvolved using the DeltaVision software (Applied Precision). Confocal images were captured with a Zeiss 510 or a Zeiss 710 laser-scanning confocal microscope.

To achieve spatially defined photoactivation of PA-GFP in the Z-axis, a Ti:sapphire two-photon laser (1,600–1,800 mW Chameleon Ultra, Coherent Scientific) tuned at 775 nm was used[61]. For actin studies, apical and lateral region of cells were identified with the mRFP signal of mRFP–PA-GFP–actin and mCherry–K-Ras^{C14}, respectively. PA-GFP fluorescence was activated using a constant region of interest (ROI, 3.5 μm × 1.05 μm) at either of these regions by a single scan with infrared laser irradiation (30% transmission), and time-lapse images of photoactivated GFP were captured every ∼250 ms in a 5.6 μm × 2.8 μm ROI using a $\times 60$ plan Apo 1.4 NA objective at $\times 4$ digital zoom and appropriate filter sets to capture GFP fluorescence.

To track selected E-cadherin populations, mEcad–mRFP–PA-GFP was photoactivated either at the apical or lateral regions with a 405 nm, 30 mW laser at 1% transmission on a LSM 710 Zeiss confocal microscope. Time-lapse images of photoactivated GFP and mRFP fluorescence were acquired at 30 s intervals using a $\times 40$ objective, 1.3 NA oil Plan-Apochromat immersion lens at 6× digital magnification and six Z-stacks of 0.48 μm step size.

Antibodies and inhibitors. Primary antibodies in this study were: mouse monoclonal antibody HECD-1 against the ectodomain of E-cadherin (1:50; clone# NCC-CAD-299, a gift from P. Wheelock, University of Nebraska, Omaha, USA, with the permission of M. Takeichi); rat monoclonal antibody against the ectodomain of E-cadherin (1:50; Invitrogen; catalogue number 13-1800, clone number ECCD-1); mouse monoclonal antibody against the cytoplasmic domain of E-cadherin (1:1,000; Transduction Laboratories; catalogue number 610182, clone number 36); rabbit antibody against either non-muscle myosin heavy chain IIA (NMIIA, also known as MYH9) or non-muscle myosin heavy chain IIB (NMIIB, also known as MYH10) (1 in 500; Covance; catalogue number PRB-440P, polyclonal and catalogue number PRB-445P-100, polyclonal respectively); mouse monoclonal antibody against myosin IIB heavy chain (1:50; DSHB; The University of Iowa); mouse monoclonal antibody against GFP (1:1,000; ROCHE; catalogue number 11814460001, mixture of clones 7.1 and 13.1); mouse monoclonal antibody against Arp3 (1:1,000; Sigma; catalogue number A5979, clone FMS338); sheep antibody

against Arp3 (1:1,000; Cytoskeleton; catalogue number AAR01-A, polyclonal); rabbit polyclonal antibody against ArpC2 (p34; 1:1,000); mouse monoclonal antibody against actin (1:100; Millipore; catalogue number MAB1501, clone number C4); rabbit monoclonal antibody 30D10 against N-WASP (1:50; Cell Signaling Technologies; catalogue number 4848, clone number 30D10); rabbit antibody against GAPDH (1 in 4,000; Trevigen; catalogue number 2275-PC-100; polyclonal); rabbit antibody against WIRE (1:50; HPA024467; Sigma Aldrich, catalogue number 4848, polyclonal). Secondary antibodies were species-specific antibodies conjugated with either AlexaFluor 488, 546 or 647, used at a dilution of 1:1,000 for immunofluorescence (Molecular Probes, Life Technologies), or with horseradish peroxidase antibodies used at 1:1,000 for immunoblotting (Bio-Rad Laboratories). Cells were incubated with human transferrin–AlexaFluor 546 conjugate (Molecular Probes) diluted at 1:500 in serum-free media for an hour. Media were then changed for live-cell imaging.

ROCK inhibitor Y-27632 (30 μM, Sigma-Aldrich), jasplakinolide (0.2 μM, Merck) and latrunculin-A (1 μM, Sigma-Aldrich) were applied for 15–30 min.

Plasmids, siRNA and shRNA. The lentivirus expression vector LentiLox pLL5.0 (backbone pLL3.7) and the third-generation packaging constructs pMDLg/pRRE, RSV–Rev and pMD.G were gifts from J. Bear (UNC Chapel Hill, USA). mRFP–PA-GFP–actin was provided by G. Charras (UCL, UK). Cav1–GFP was provided by A. Helenius (Institute of Biochemistry, ETH Zurich, Zurich, Switzerland)[62]. ptdTomato (ptdT)–C1 was provided by R. Tsien (UCSD, USA). pCS2.0 vector with GFP fused to the calponin homology domain of utrophin (GFP–UtrCH) was a gift from B. Bement (UW-Madison, USA). pCS2.0 Tag-RFP-T–UtrCH was generated by subcloning Tag-RFP-T (ref. 63; a gift from A. Lichius, Fungal Genetics Stock Center) into BamHI/BspEI sites within the GFP–UtrCH construct. mCherry–2xFYVE was a gift from J. Stow (Institute for Molecular Bioscience, University of Queensland, Australia). pLL5.0 E-cadherin shRNA/Ecad–tdT, pLL5.0 E-cadherin shRNA/mEcad–mCherry and pLL5.0 E-cadherin shRNA/mE-cadherin–mRFP–PA-GFP were generated by subcloning tdT, mCherry and mRFP–PA-GFP respectively into AgeI/SbfI-digested pLL5.0 E-cadherin shRNA/mEcad–GFP. pLL5.0 N-WASP shRNA/GFP and pLL5.0 N-WASP shRNA/mCherry lentiviral vectors were described previously[19].

pLL5.0 mCherry–K-Ras^{C14}, pLL5.0 MYH9 shRNA/mCherry–K-Ras^{C14} and pLL5.0 MYH10 shRNA/mCherry–K-Ras^{C14} were generated by introducing the annealed oligonucleotide from the carboxy-terminal 14 amino acid region of human K-Ras (NM_004985.3 K–Ras^{C14}; ref. 64) into BsrGI-digested pLL5.0 Cherry, pLL5.0 MYH9 shRNA/Cherry and pLL5.0 shMYH10/Cherry respectively. pEcad–GFP–N-WASP$^{\Delta VCA}$ was generated by recombining mEcad–GFP, a linker (5′-GGGTCTACATCTGGATCTGGGAAGCCGGGTTCTGGTGAGGGTTCT-3′) and N-WASP$^{\Delta VCA}$ into a NotI/AgeI-digested pEGFP–N1 vector using the In-Fusion HD Cloning Kit (Clontech). pLL5.0 E-cadherin shRNA/Ecad–GFP–N-WASP$^{\Delta VCA}$ was generated by introducing mEcad–GFP–N-WASP$^{\Delta VCA}$ from pEcad–GFP–N-WASP$^{\Delta VCA}$ into the EcoRI/SbfI-digested pLL5.0 E-cadherin shRNA/mEcad–GFP using the In-Fusion HD Cloning Kit (Clontech). GFP–H-Ras^{V12} was previously described[65]. pLL5.0 E-cadherin shRNA/Ecad–GFP–IRES–HA–H-Ras^{V12} was generated by recombining both IRES and HA-tagged H-Ras^{V12} into SbfI-digested pLL5.0 E-cadherin shRNA/mEcad–GFP.

Algorithms from Dharmacon were used to generate RNAi sequences against the 3′UTR of MYH9 (NM_002473) and 3′UTR of MYH10 (NM_005964). MYH9 shRNA against 5′-CACAAAGGAGTGAGTGAAA-3′ and MYH10 shRNA against 5′-CAATACAGTGGGACAGTTA-3′ were cloned into HpaI/XhoI-digested pLL5.0 Tag-RFP-T–UtrCH. E-cadherin and ArpC2 (p34) were silenced with Dharmacon SMARTpool siRNA (50 nM) directed against human CDH1 (NM_004360; target sequences: 5′-GGCCUGAAGUGACUCGUAA-3′; 5′-GAGAACGCAUUGCCACAUA-3′; 5′-GGGACAACGUUUAUUACUA-3′; 5′-GACAAUGGUCCUCCAGUUG-3′), human ArpC2 (NM152862; NM005731; target sequences: 5′-GUACGGGAGUUUCUUGGUA-3′; 5′-GGACAGAGUCACAGU-AGUC-3′; 5′-GCUCUAAGGCCUAUAUUCA-3′; 5′-CCAUGUAUGUUGAGUC-UAA-3′) and N-WASP (NM003941; target sequences: 5′-CAGCAGAUCGGAAC-UGUAU-3′; 5′-UAGAGAGGGUGCUCAGCUA-3′; 5′-GGUGUUGCUUGUCUU-GUUA-3′; 5′-CCAGAAAUCACAACAAAUA-3′) respectively.

Lentivirus production and transduction were performed as described previously[13,66].

Laser nanoscissors. Nanoscissors experiments were performed on a LSM 510 meta Zeiss confocal microscope equipped with a $37\,^{\circ}C$ heating stage. Images (266×266 pixels, 0.14 μm per pixel) were acquired with a $\times 63$ objective, 1.4 NA oil Plan Apochromat immersion lens at $\times 2$ digital magnification. Time-lapse images were acquired 4 frames after ablation with an interval of 8 s per frame. The Ti:sapphire

laser (Chameleon Ultra, Coherent Scientific) was tuned to 790 nm for the ablation of cell–cell contacts labelled with either Ecad–GFP or Ecad–TdT. A constant ROI, $3.8 \times 0.6\,\mu m$ with the longer axis orthogonal to the cell–cell contact, was ablated with 30 iterations of the 790 nm laser at 18% transmission. The distance (d) between vertices that define the ablated contact was measured as a function of time (t) using the MTrackJ-ImageJ plugin. Distance values after ablation were subtracted from the initial contact length, $d(0)$. The values of $d(t) - d(0)$ were averaged across technical replicates at each time point and biological replicates were obtained for each experimental group. These mean values were plotted against time to obtain the initial recoil curves.

The instantaneous recoil (rate of recoil at $t = 0\,s$) was then determined by fitting the following model to the data:

$$d(t) - d(0) = \frac{\text{initial recoil}}{k} \cdot \left(1 - e^{-kt}\right)$$

The model was fitted with the nonlinear least-squares algorithm nls in the R statistical programming language (R Foundation for Statistical Computing, Vienna, Austria. http://www.R-project.org/). To test for a significant difference in initial recoil between two treatment groups, the following model was fitted to the combined data:

$$d(t) - d(0) = \begin{cases} \frac{\text{Initial recoil}_1}{k_1} \cdot \left(1 - e^{-k_1 t}\right), & \text{1st group,} \\ \frac{\text{Initial recoil}_1 + \text{initial recoil}_\Delta}{k_2} \cdot \left(1 - e^{-k_2 t}\right), & \text{2nd group} \end{cases}$$

The P value for the parameter initial recoil$_\Delta$ indicates whether there is evidence for a significant difference in the initial recoil rate between the groups.

Image processing and analysis. The images presented were processed with ImageJ (http://rsb.info.nih.gov/ij/) and Photoshop CS (Adobe Systems). A rolling-ball (5 pixels) background subtraction and median filter of one pixel radius was sequentially applied on the original Z-stacks which were then Z-projected as a sum of slices and image size increased for representation purposes. For the Videos presented, a bleach correction simple ratio function (Image J Plug-in, J. Rietdorf, EMBL Heidelberg) was applied to correct for photobleaching. Image size was then increased to smoothen Videos on conversion into the H.264 compression format. The edges of XZ images in extrusion studies were increased using the ImageJ canvas size function to uniformly align images for representation purposes.

For three-dimensional co-localization analysis, deconvolved images of $0.1\,\mu m \times 0.1\,\mu m \times 0.2\,\mu m$, xyz pixel resolution were background subtracted and converted into 8 bits and an intensity cutoff was applied to further remove nonspecific signal. The images were then processed for object-based co-localization analysis[30] (OBCOL) using default parameters except for watershed tolerance (10) and size cutoff to remove noise (<20 voxels volume). For the co-localization analysis, spots with an overlap of 3 voxels or more between fluorescent channels were registered as a positive co-localized cluster. Analysis of the negative control was performed on OBCOL-processed images with randomized Z positions generated by a Stack-slice Manipulation plugin on ImageJ (B. Dougherty). The numbers of co-localized Ecad clusters were then expressed over the total number of junctional Ecad clusters. Graphs and statistical analysis were performed using Prism (GraphPad Software).

For Ecad cluster density cross-correlation, at the lateral interface of cells expressing either Ecad–GFP or Ecad–tdT, the lateral clusters were segmented from raw images with OBCOL as described above and then projected into 2D (sum-slices) images. Cross-correlation of Ecad–GFP and Ecad–tdT cluster density fluctuations within multiple $1\,\mu m^2$ windows was measured and Pearson's correlation coefficient between Ecad–GFP and Ecad–tdT cluster density measurements was analysed in Prism.

F-actin intensity fluctuations were measured within multiple $1\,\mu m^2$ windows and the pooled variance derived for control, NMIIA RNAi and NMIIB RNAi.

For cluster tracking, radial velocity and Fourier analysis, segmentation of junctional Ecad into distinct Ecad spots was performed with OBCOL. Tracking of Ecad clusters was performed with MtrackJ (ref. 33) and the position (x_t, y_t) of Ecad clusters recorded over time. To avoid analysing nonspecific particles and vesicles, only Ecad spots that reside at the junction throughout the entire duration of the Videos were analysed. The position (x_0, y_0) of the Ecad cluster in the first frame of time-lapse images was fixed as the original position. Subsequent radial displacements at each time point relative to this position were then extracted from the particle tracking data and calculated as $d_t = \sqrt{(x_t - x_0)^2 + (y_t - y_0)^2}$. To extract Ecad cluster radial velocity, instantaneous radial displacement differences $(d_{t+\Delta t} - d_t)$ with $\Delta t = 10\text{–}15\,s$ were obtained and a second-order smoothing of

3 neighbours (by averaging) was then applied on these values to reduce noise from particle tracking. The radial velocity graphs illustrating the direction and speed of Ecad cluster motion were obtained by plotting radial velocity against time. Fast Fourier transformation was then applied on the tracking data to decompose Ecad oscillatory motion into a spectrum of power amplitude distributed over a range of frequencies, as described previously[20]. A Gaussian curve was then fitted to the pooled power spectrum plot to extract the amplitude at the dominant frequency, which corresponds to the period of Ecad cluster oscillations ($\sim$111 s). Mean square displacement (MSD): average d_t^2 values were obtained and plotted against time.

For control for tracking analysis in Z-projections (Supplementary Fig. 2c–e), cluster tracking and velocity analysis were performed on Z-projections of three-dimensional time-lapse images. In *en face* images, lateral regions of cells are tilted to different extents and it was possible that the tracking measurements on these projections differed from their true distance values. To test the effects of contact inclination on our tracking analysis, we fitted the MSD of cadherin clusters to mono-exponential functions and performed simulations to measure the impact of contact inclination on our tracking measurements. Two-way analysis of variance (ANOVA) between MSD of simulated data showed that contact inclination had no significant impact on MSD values (data not shown), unless measurements were obtained after 130 s and on contacts tilted by more than 70° ($P < 0.05$). As the instantaneous displacements were obtained from Videos with $\sim$10–15 s time intervals, we expect that our velocity measurements were not affected by the degree of contact inclination. In agreement with the simulations, we were unable to find significant differences between MSD at 130 s ($P > 0.05$, $n = 9$, t-test, data not shown) and instantaneous displacements of cadherin clusters located on slanted or perfectly planar regions ($P > 0.999$; two-way ANOVA).

For correlation analysis of F-actin density and Ecad cluster distance, mosaic expression of the actin-binding domain of utrophin fused to GFP (GFP–Utr) allowed detailed analysis of junctional F-actin organization within a single cell in a monolayer, uncomplicated by F-actin signals from the neighbouring cells and other cellular regions. From these Ecad–tdT/GFP–UtrCH dual-colour time-lapse images, a line was then drawn between Ecad clusters connected by a F-actin cable. ImageJ ROI Manager was used to record the position of the F-actin cable and to measure the distance between Ecad clusters and the mean GFP–UtrCH fluorescence intensity (F-actin cable density) in all subsequent frames. The start of a contraction of an F-actin cable is defined as the first event where the mean GFP–UtrCH fluorescence intensity along the line exceeded the average GFP–UtrCH fluorescence intensity measured for the same pair of Ecad clusters for the whole Video. The subsequent changes of the distance measurements between Ecad clusters and the mean intensity values of the F-actin cable were both normalized to their respective maximum values. These values were then plotted against time in Prism.

For quantification of F-actin cable number and lifetime, to remove nonspecific background, we set intensity values one standard deviation below the mean lateral F-actin (Tag-RFP-T–UtrCH) intensity to zero. An intensity threshold was then applied to binarize the F-actin cables and the duration for which an intact F-actin cable connects Ecad clusters was measured for multiple cables to obtain the lifetime of F-actin cables.

For quantification of junctional fluorescent density and line-scan analysis, either apical or lateral Ecad was outlined with the basal region of cells avoided. The mean intensity of the selected junctional region was then measured from the raw deconvoluted images. Line-scan analysis was performed as described previously[28].

Statistics and repeatability of experiments. For analysis, standard deviation from initial trials was determined and used to determine sample size based on confidence interval calculations at confidence levels of 95%. Only the analyses of cell extrusion involved more detailed inclusion/exclusion criteria and are described in the Methods above (Cell Culture and Transfection). These inclusion/exclusion criteria were pre-established before performing the quantification.

Randomization was not used in the entire study. The control and treated groups of cells came from the same source and conclusions that were made in the manuscript were based on comparison of groups with data of similar variances. In addition, conclusions derived from the data in this manuscript meet the assumptions of the test and all have a normal distribution. A third party with no previous knowledge of the hypothesis aided in the quantification of Ecad oscillations and F-actin cable characterization. For all other studies in the manuscript, the investigators were not blinded to allocation during experiments and outcome assessment.

The numbers of independent experiments performed for all of the quantitative data are indicated in the figure legends. All supplementary videos and representative images in Figs 1a, 2a,c,e,f,g, 3a,f, 4c,f,h,l, 5a,d, 6a,c,d, 7c and 8a,e,h,j and Supplementary Figs 1b–d, 2b, 3a, 4a,b, 5a and 6f were observed in three independent

experiments except for Fig. 7b and Supplementary Fig. 9, which were repeated twice. In addition, Fig. 1b,c and Supplementary Fig. 1c,d have been routinely reported by the laboratory (in a total of more than 8 independent experiments). Figures 1a and 3a and Supplementary Videos 10 and 12 represent *en face* contacts of cells expressing GFP–UtrCH, where the lateral contact is in contact with neighbouring cells that were not expressing GFP–UtrCH. This prevents the complication of GFP–UtrCH signal from other subcellular regions of the monolayer.

Similar apicolateral patterns of cadherin/actin staining were reported previously by others[26] and similar patterns of lateral cadherin movement have also been reported in other cell lines[24]. The apical concentrations of N-WASP shown in Fig. 6c,d were routinely observed in the laboratory and reported previously in three-dimensional cyst cultures[48]. The observation of apical extrusion in cells expressing H-Ras[V12] mosaically within the epithelium rather than basal extrusion was also reported previously in confluent MDCK monolayer and in zebrafish[13].

61. Schneider, M., Barozzi, S., Testa, I., Faretta, M. & Diaspro, A. Two-photon activation and excitation properties of PA-GFP in the 720-920-nm region. *Biophys. J.* **89,** 1346–1352 (2005).

62. Pelkmans, L., Kartenbeck, J. & Helenius, A. Caveolar endocytosis of simian virus 40 reveals a new two-step vesicular-transport pathway to the ER. *Nat. Cell Biol.* **3,** 473–483 (2001).

63. Lichius, A. & Read, N. A versatile set of Lifeact-RFP expression plasmids for live-cell imaging of F-actin in filamentous fungi. *Fungal Genet. Rep.* **57,** 8–14 (2011).

64. Gomez, G. A. & Daniotti, J. L. H-Ras dynamically interacts with recycling endosomes in CHO-K1 cells: involvement of Rab5 and Rab11 in the trafficking of H-Ras to this pericentriolar endocytic compartment. *J. Biol. Chem.* **280,** 34997–35010 (2005).

65. Prior, I. A. *et al.* GTP-dependent segregation of H-ras from lipid rafts is required for biological activity. *Nat. Cell Biol.* **3,** 368–375 (2001).

66. Priya, R. & Gomez, G. Measurement of junctional protein dynamics using fluorescence recovery after photobleaching (FRAP). *Bio-protocol* (2013).
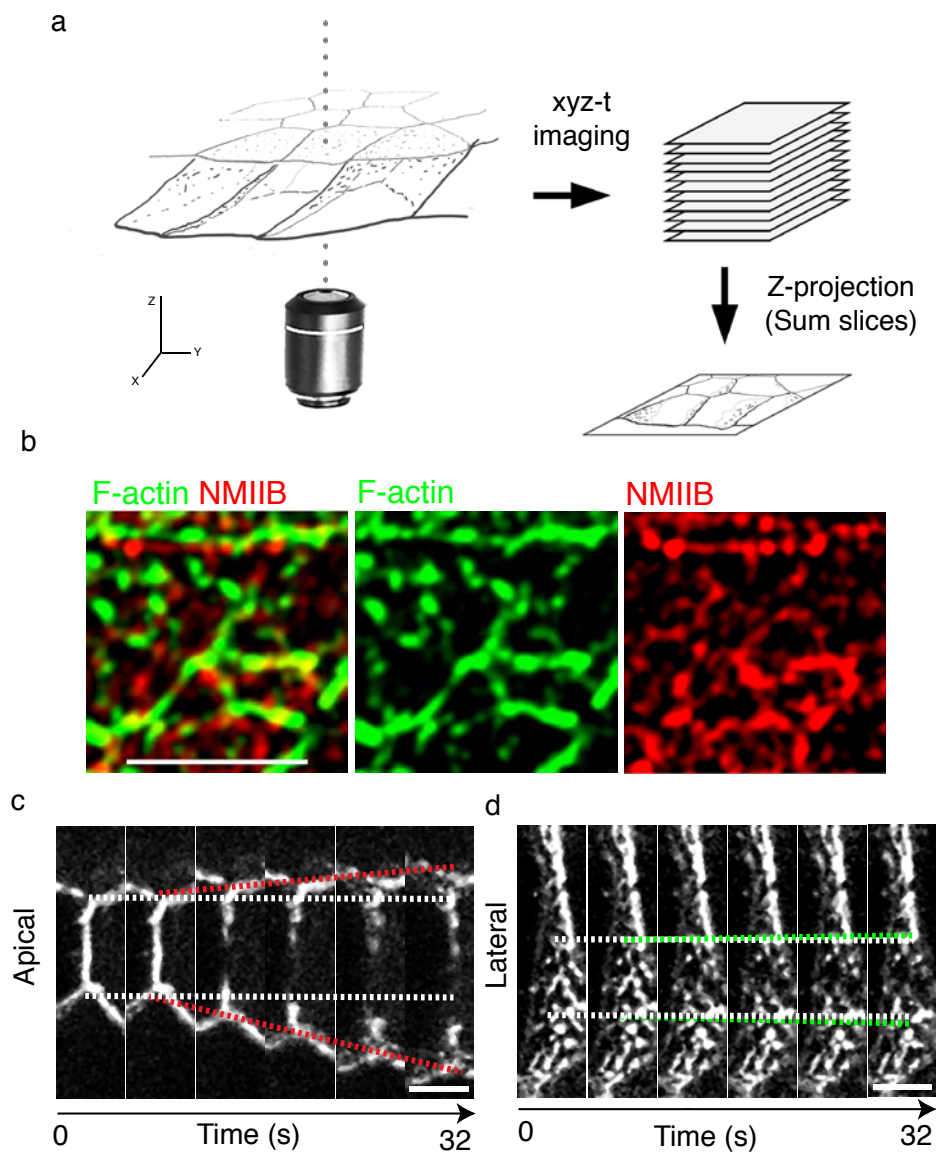
Supplementary Figure 1 Regional disparity in apical and lateral junctional tension. **a,** Cartoon of apicolateral imaging at slanted (en face) cell-cell contacts. b, Representative image at the cell-cell contact of cells expressing GFP-UtrCH (F-actin, green) and immunostained for Myosin IIB (red). c, d, Representative confocal images at various time points before and after nanoablation at either apical (c) or lateral (d) regions of cell-cell contacts. Scale bars: 5 μm.
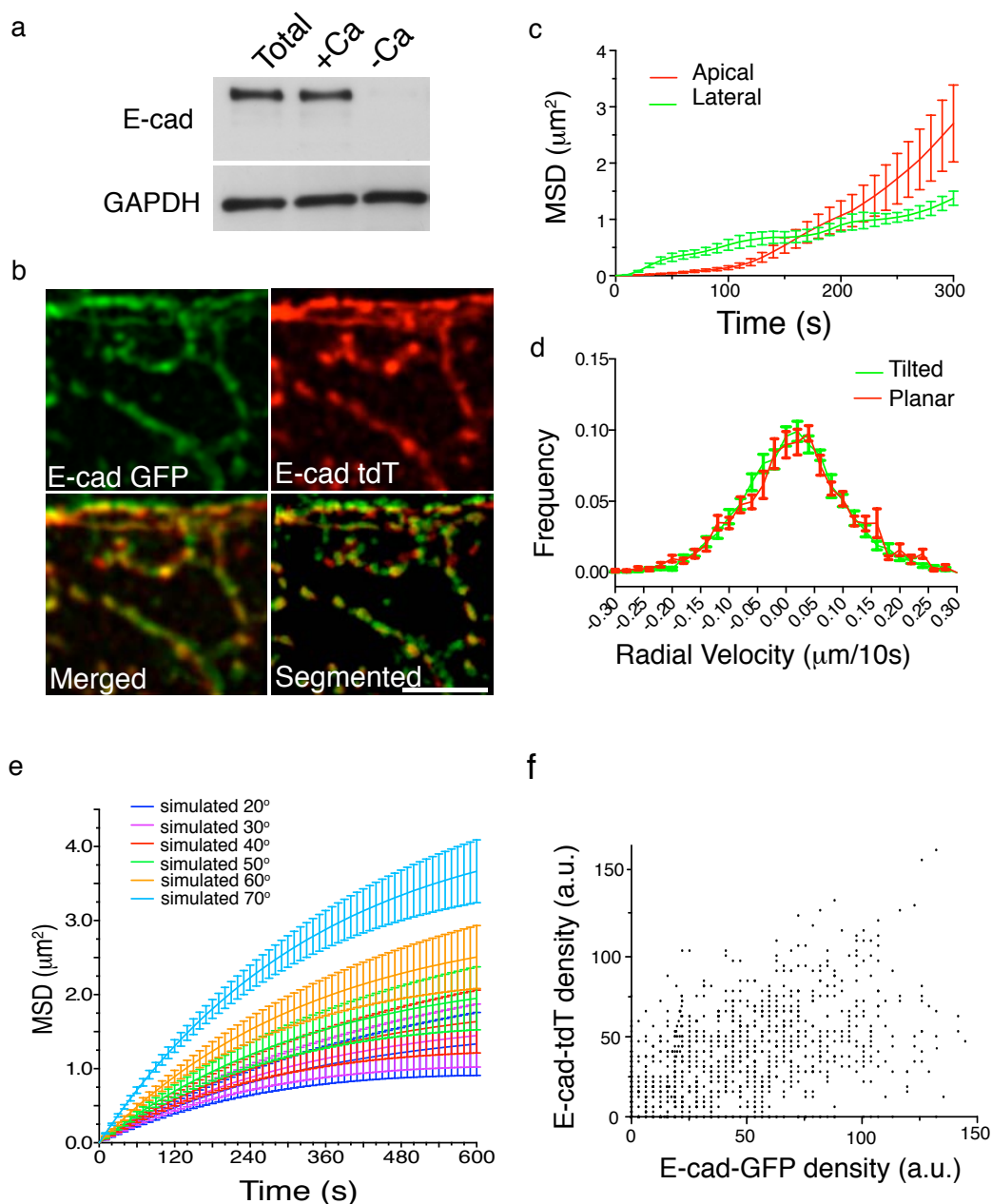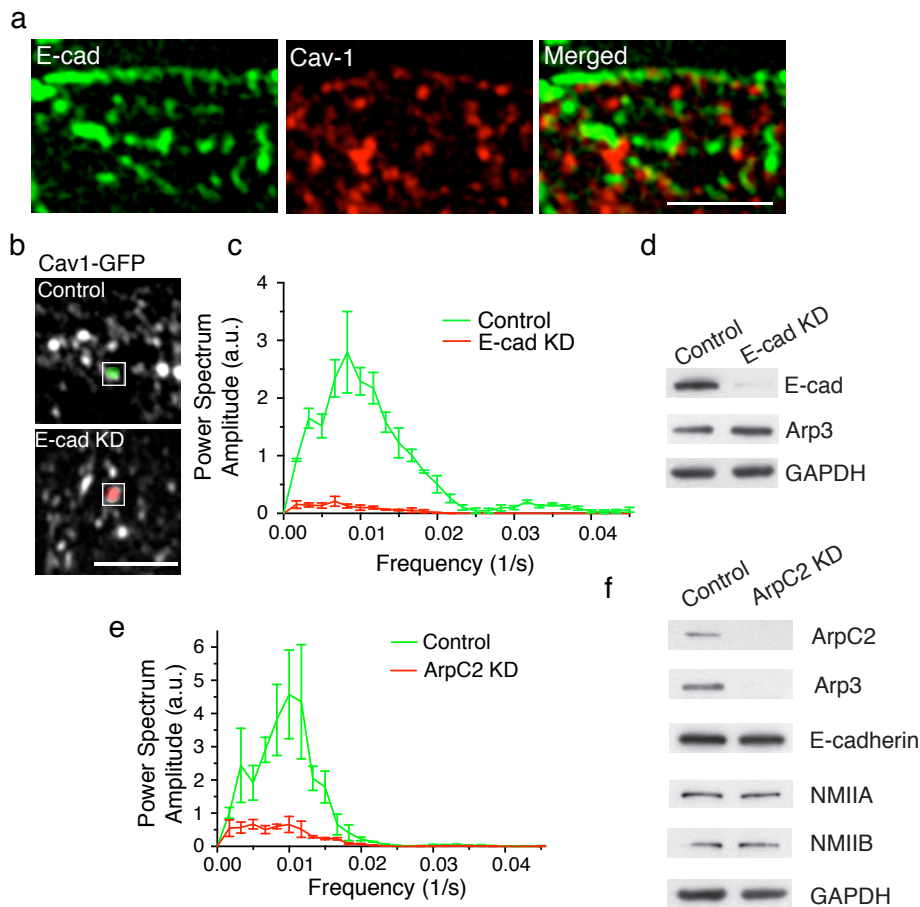
Supplementary Figure 2 Dynamic lateral E-cadherins are trans-interacting clusters. a, Surface expression of E-cadherin was measured with trypsin protection assays. Cells were lysed immediately (Total) or after trypsinisation in the presence (+Ca) or absence (–Ca) of extracellular calcium. Cell lysates were immunoblotted for E-cadherin and GAPDH. Uncropped images of blots are shown in Supplementary Figure 9. b, Representative immunofluorescence images of the interface between Ecad-GFP and Ecad-tdTomato cells, and the corresponding merged image segmented by OBCOL to resolve individual E-cad clusters. c, Mean square displacement (MSD) of apical and lateral cadherin clusters. d,e, Radial velocity distribution of

E-cad clusters in planar and tilted contacts (d). Effect of contact inclination on Mean Square Displacement (MSD) measurements of E-cadherin clusters (e). Simulation of tracking data to produce MSD values at 20°, 30°, 40°, 50°, 60° and 70° tilt angles respectively. f, Pooled density fluctuations of E-cad clusters within $1\mu m^2$ regions of analysis at the lateral interfaces of Ecad-GFP and Ecad-tdTomato expressing cells (average Pearson's coefficient= 0.67). Data are means±SEM calculated from n= 9 individual cell-cell contacts (28 individual cadherin clusters) from 2 independent experiments (statistical information and source data in Supplementary Data 1). Scale bars: 5 µm.
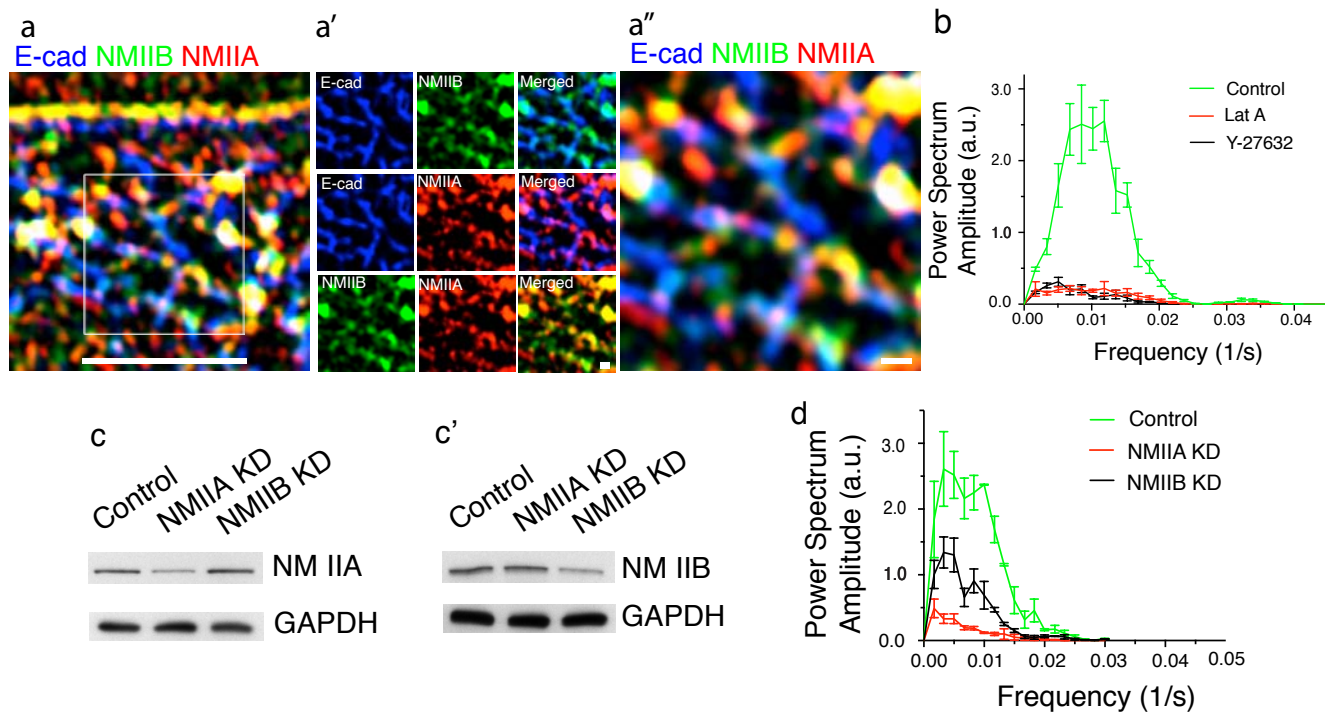
Supplementary Figure 3 Actomyosin network exerts contractile forces on lateral E-cad clusters. a, Immunofluorescence image (a, merged, a', in detail) of cell-cell contact immunostained for E-cad (blue), Myosin IIA (red) and Myosin IIB (green). A high magnification view (a'') of the indicated area in a is shown. b, F-actin integrity and active myosin support lateral cadherin oscillations. Fourier analysis of lateral E-cad after treatment with DMSO (Control, green), latrunculin A (Lat A, red) or Y-27632 (black). Power spectrum amplitude for the full-range of frequencies are shown. c, c', Myosin IIA (c) or Myosin IIB (c') with GAPDH (loading control) immunoblots of lysates from control, Myosin IIA KD and Myosin IIB KD cells. Uncropped images of blots are shown in Supplementary Figure 9. d, Myosin II isoforms support lateral cadherin oscillations. Power spectrum amplitude for the full-range of frequencies from Fourier analysis of lateral E-cadherin radial velocity in cells expressing either pLL5.0 empty vector (Control, green), shRNA against Myosin IIA (NMIIA KD, red) or shRNA against Myosin IIB (NMIIB KD, black). All data are means±SEM calculated from n=3 independent experiments (statistical information and source data in Supplementary Data 1). Scale bars: (a) 5 μm, (a',a''), 0.5 μm.

Supplementary Figure 4 E-cadherin supports junctional contractility through Arp2/3 based actomyosin assembly. a, Ecad-GFP and Caveolin-1-mCherry expressed at the lateral junctions do not colocalize from Supplementary video 4. b, c, Representative images of Caveolin-1-GFP (Cav1-GFP, b) and power spectrum obtained from Fourier analysis of Cav-1-GFP puncta radial velocity (c) at the lateral junctions in control (green) and E-cadherin knockdown cells (E-cad KD, red). d, E-cad, Arp3 and GAPDH (loading control) immunoblots of lysates from control or E-cadherin KD cells. e, Fourier analysis of lateral E-cadherin in control (green) or ArpC2 knockdown (red) cells. f, ArpC2, Arp3, E-cadherin, Myosin IIA, Myosin IIB and GAPDH (loading control) immunoblots of lysates from control or ArpC2 knockdown cells. Uncropped images of blots in (d) and (f) are shown in Supplementary Figure 9. All data are means±SEM calculated from n= 3 independent experiments (statistical information and source data in Supplementary Table 1). Scale bars: 5 μm.
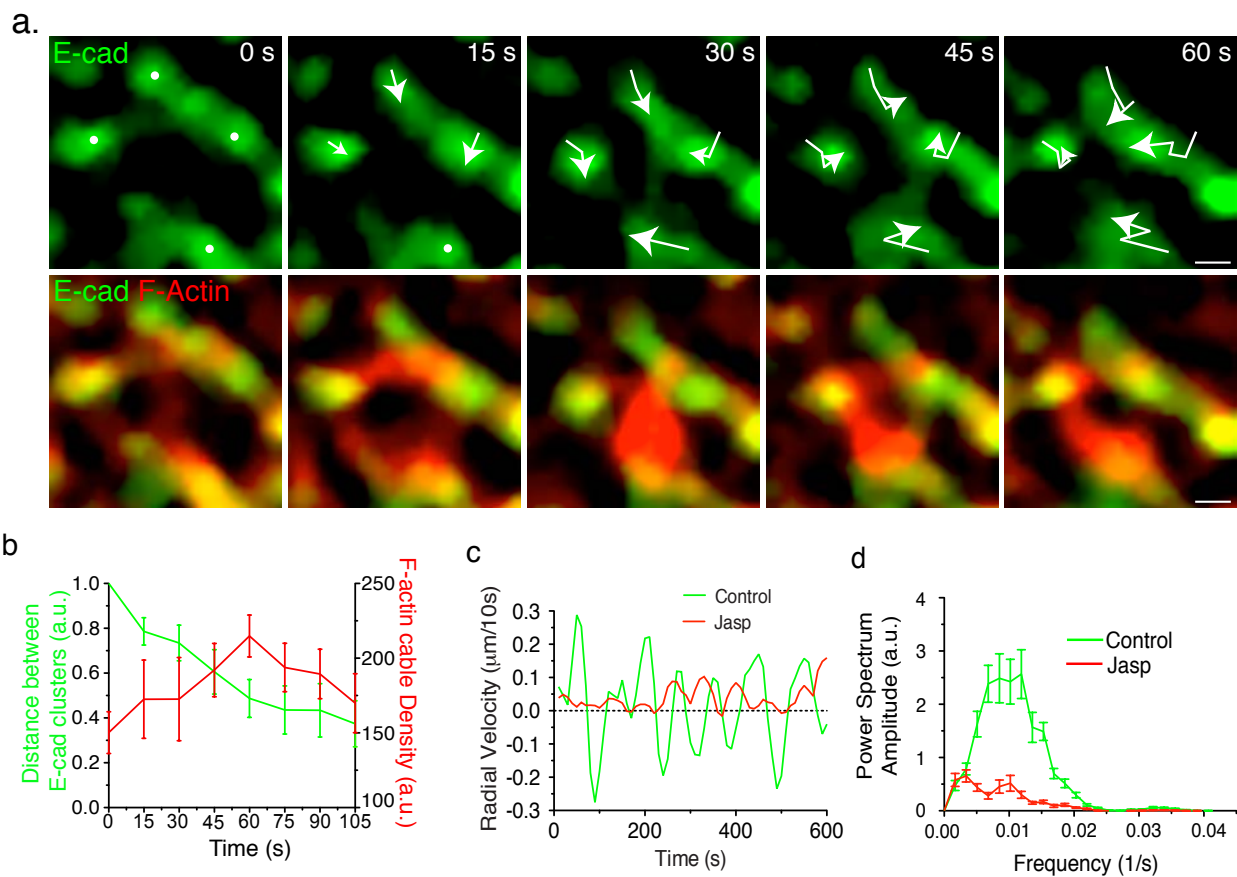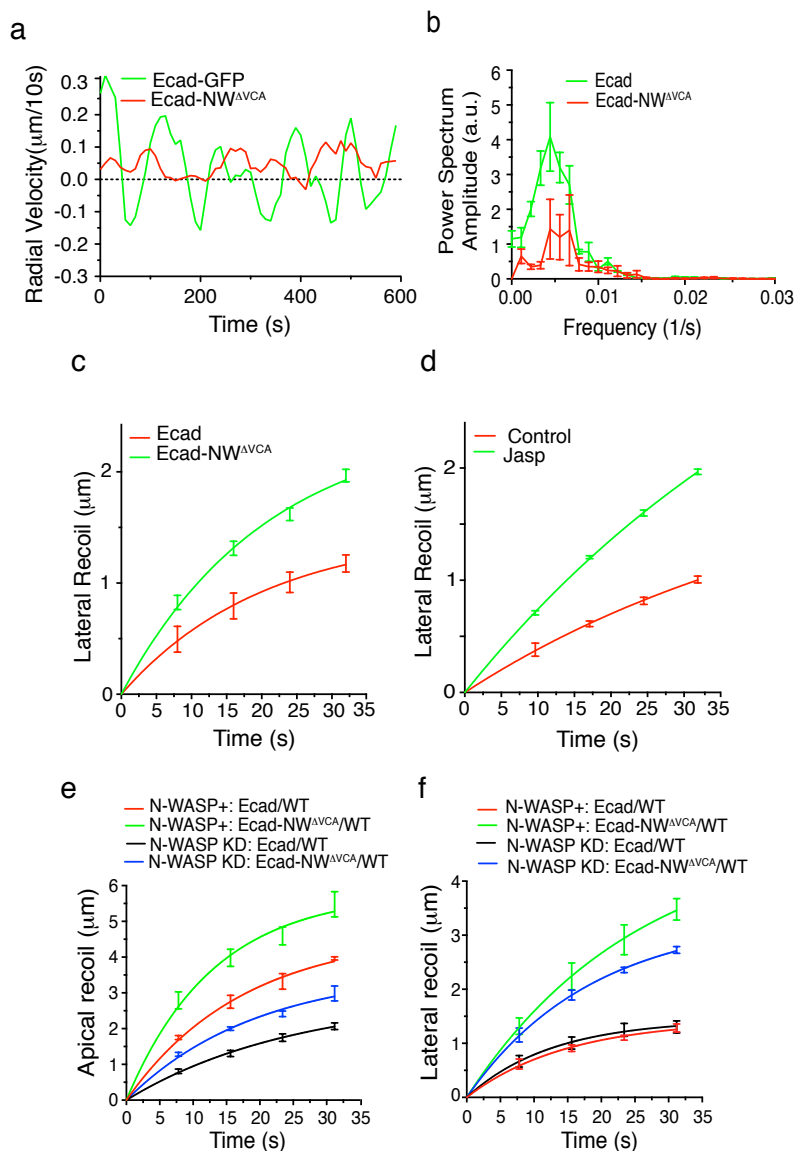
Supplementary Figure 5 Lateral F-actin turnover determines E-cad cluster oscillation. a, Time series of actin network condensation from isotropic cortical network with superimposed tracks (white) of cadherin clusters. b, Average lateral F-actin cable intensity and the corresponding normalized distances between E-cad clusters plotted against time. c, d, Jasplakinolide inhibits lateral cadherin oscillations. Representative radial velocity traces (c) and Fourier analysis (d) of lateral E-cadherin in cells treated with either DMSO (Control, green) or jasplakinolide (Jasp, red). All data are means±SEM calculated from n=3 independent experiments (statistical information and source data in Supplementary Table 1). Scale bars: 0.5 μm.
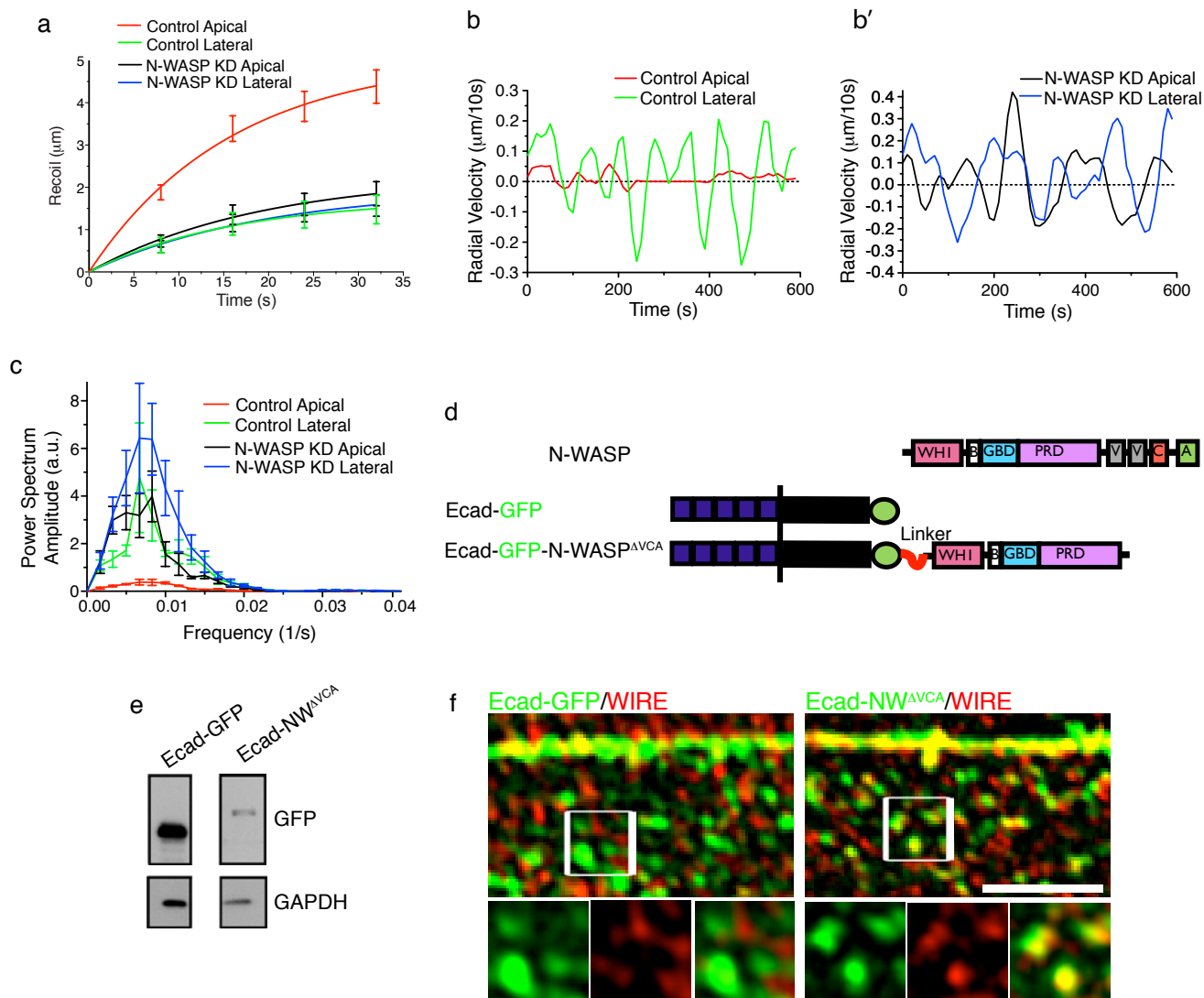
Supplementary Figure 6 N-WASP regulates junctional contractility. a, Recoil curves of apical and lateral junctions in control or N-WASP KD cells. b, b', Representative radial velocity traces of apical (red: Control Apical, black: N-WASP KD Apical) or lateral (green: Control Lateral, blue: N-WASP KD Lateral) E-cad in cells transduced with lentivirus bearing either pLL5.0 empty vector (b) or shRNA against N-WASP (b'). c, Fourier analysis and power spectrum amplitude for the full-range of frequencies of ZA and lateral E-cad cluster radial velocity in control and N-WASP knockdown cells. d, Schematic of Ecad-GFP-N-WASP$^{\Delta VCA}$ fusion protein. e, GFP and GAPDH (loading control) immunoblots of lysates from Ecad-GFP and E-cad-GFP-N-WASP$^{\Delta VCA}$ cells. Uncropped images of blots are shown in Supplementary Figure 9. f, Representative images of junctional Ecad-GFP, E-cad-GFP-N-WASP$^{\Delta VCA}$ and WIRE. Lower detailed panels show colocalization of lateral E-cad-GFP-N-WASP$^{\Delta VCA}$ with WIRE. However, lateral Ecad-GFP does not colocalize with WIRE. Scale bars are 5 μm except for magnified view: 0.5 μm. All data are means±SEM calculated from n=3 independent experiments except for (a) which were technical replicates (means±SD, n=19 contacts) from one out of two independent experiments (statistical information and source data in Supplementary Table 1).

Supplementary Figure 7 N-WASP$^{\Delta VCA}$ promotes junctional contractility by F-actin stabilization. a, b, Representative radial velocity traces (a) and Fourier analysis (b) of both lateral Ecad-GFP and Ecad-GFP-N-WASP$^{\Delta VCA}$. c, Recoil of the lateral junctions of Ecad-GFP and Ecad-GFP-N-WASP$^{\Delta VCA}$ expressing monolayer. d, Lateral recoil in DMSO (Control) or Jasplakinolide (Jasp) treated cells. e, f, Recoil at apical (e) and lateral (f) interfaces of cells either expressing Ecad-GFP/WT or Ecad-GFP-N-WASP$^{\Delta VCA}$/WT in N-WASP+ or N-WASP KD monolayer. All data are means±SEM; calculated from n= 3 independent experiments (statistical information and source data in Supplementary Table 1).
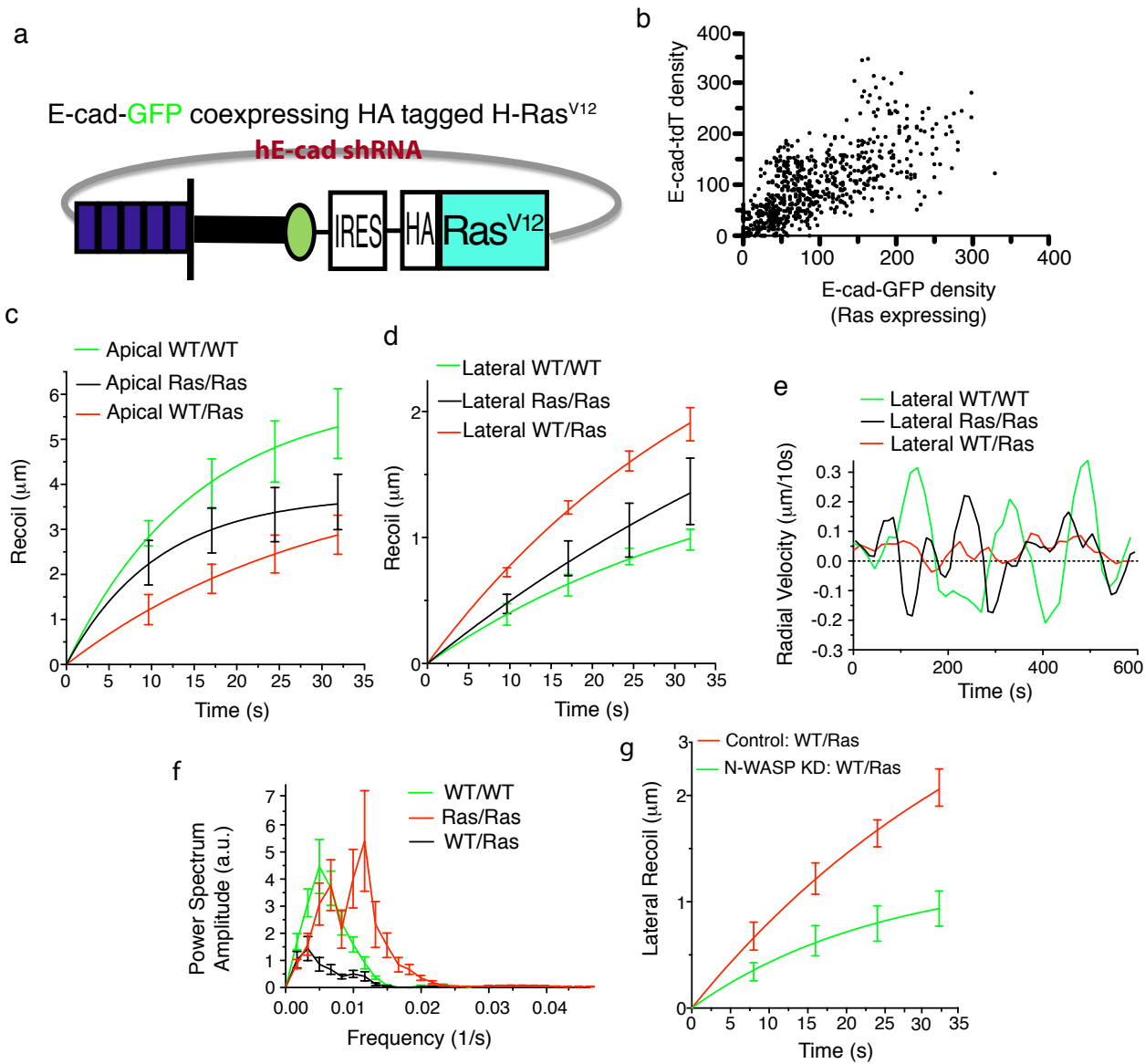
Supplementary Figure 8 Characterization of junctional contractility at the interface of WT/WT, H-Ras^{V12}/H-Ras^{V12} and WT/ H-Ras^{V12} cells. a, Design of a HA-tagged H-Ras^{V12} construct co-expressing Ecad-GFP and E-cad shRNA in the pLL5.0 vector by introduction of an IRES sequence. b, E-cadherin trans-interactions are unaffected at the interface of wild-type and transformed cells. Pooled density fluctuations of E-cad clusters within 1µm^2 regions of analysis at the lateral interface of Ecad-GFP-IRES-HA-H-Ras^{V12} and Ecad-tdTomato expressing cell (average Pearson's coefficient=

0.74). c, d, Recoil of apical (c) and lateral (d) junctions at the interface of WT/WT, H-Ras^{V12}/H-Ras^{V12} and WT/H-RasV12. e, f, Radial velocity traces (e) and Fourier analysis (f) of lateral E-cad at the interface of WT/WT, H-Ras^{V12}/H-Ras^{V12} and WT/H-RasV12. **g**, Recoil of lateral junctions at interface between H-Ras^{V12}/WT cells in either control or N-WASP KD monolayers. All data are means±SEM; calculated from n= 3 independent experiments (statistical information and source data in Supplementary Table 1).
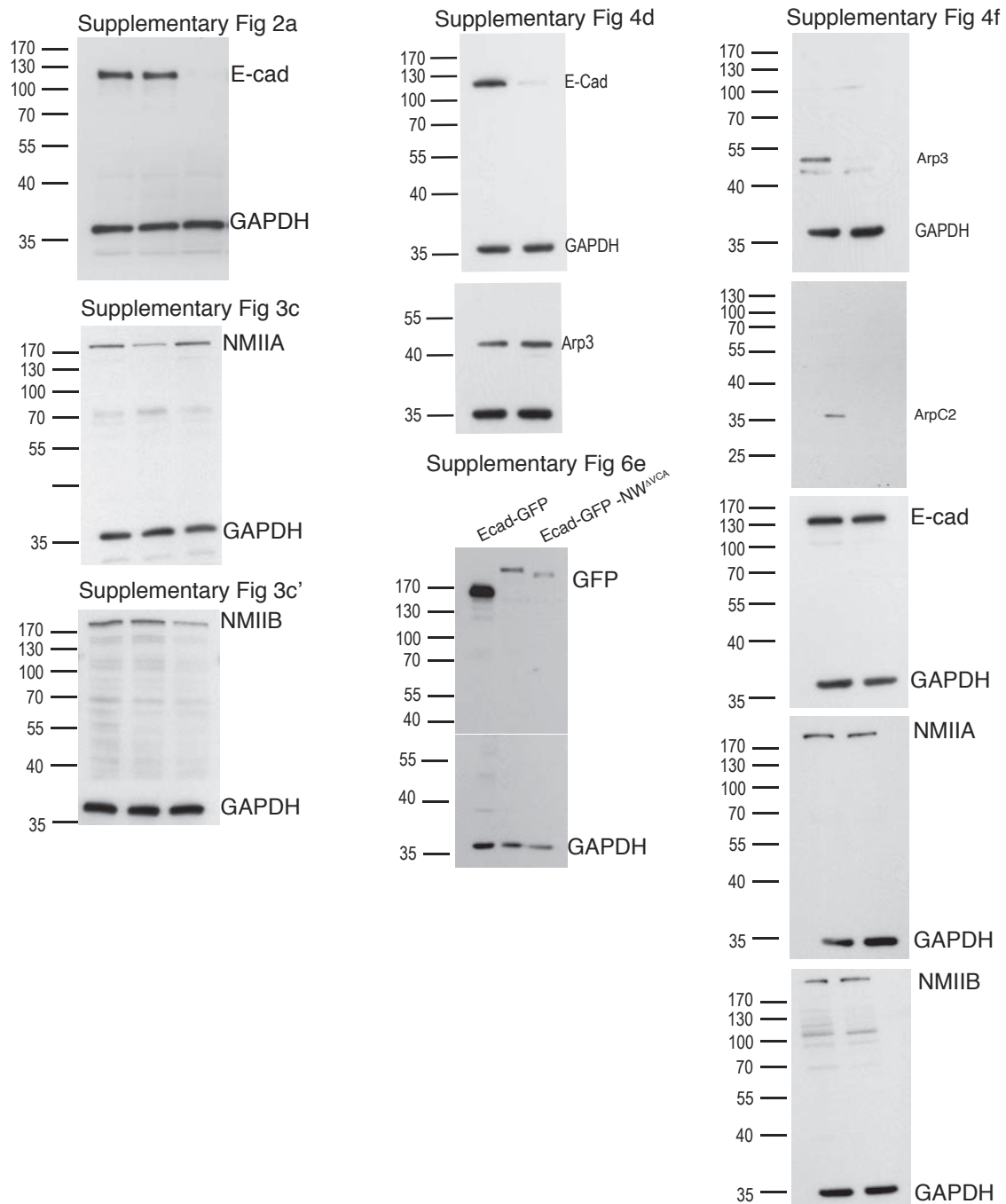
Supplementary Figure 9 Uncropped Western Blots related to Supplementary Figures 2a,3,c,c',4d,f, and 6e.

Supplemental Videos Legends

Video 1. Distinct levels of contractile tension coexist within individual E-cadherin junctions.
Nanoablation of apical and lateral cell-cell junctions in Caco-2 cells expressing Ecad-GFP in E-cad knockdown background. Arrowhead indicates the point of laser ablation with a Ti:Sapphire laser (Chameleon Ultra, Coherent Scientific, US) tuned to 790 nm. Scale bar: 5μm

Video 2. Dynamic exchange of E-cadherin between apical and lateral cell-cell contacts.
Ecad-mRFP-PA-GFP photoactivation at the lateral (upper panels) or apical (lower panels) regions of a cell-cell contact. mRFP fluorescence images are in red and activated PAGFP fluorescence is in green. Scale bar: 5μm

Video 3. E-cad clusters do not colocalize with endosomal markers.
Dual-colour time-lapse imaging of Ecad-GFP with either internalized Alexa Fluor 546 conjugated Transferrin with or mCherry-2XFYVE at cell-cell contacts. Scale bar: 5μm

Video 4. E-cad clusters and caveolin-1 puncta do not colocalize but display similar oscillatory motion.
Dual-colour time-lapse imaging of Cav1-mCherry (red) and Ecad-GFP (green) at a cell-cell contact. Scale bar: 5μm

Video 5. E-cad clusters display different patterns of movement at apical versus lateral regions of cell-cell contacts.
Live imaging of Caco-2 cells expressing Ecad-GFP in an epithelial monolayer (left). Magnified timelapse movie of an E-cad cell-cell contact (right). Note the pulsatile movement of the lateral E-cad clusters. Each image is a projection of a 6μm Z-stack. The initial still frame outlines the apical (red) and lateral (green) regions of the cell-cell contact. Scale bar: 5μm

Video 6. E-cadherin puncta represent adhesive clusters.
Mixed population of Ecad-GFP and Ecad-tdTomato expressing cells (left). Magnified timelapse movie of a lateral cell-cell contact at the interface between Ecad-GFP and Ecad-tdTomato expressing cells. Scale bar: 5μm

Video 7. Myosin II drives oscillatory fluctuations in the lateral F-actin network to drive E-cad cluster motion.
Live imaging of Caco-2 cells co-expressing Ecad-GFP (green) and TagRFP-T-UtrCH (F-actin, red) at cell-cell contacts between control, NMIIA knockdown or NMIIB knockdown cells. Upper panels show E-cadherin-GFP fluorescence images in grayscale. Scale bar: 5μm

Video 8. E-cad is required for oscillatory motion at lateral cell-cell contacts.
Time-lapse live cell imaging of Cav1-GFP at a cell-cell contact in control and E-cad RNAi cells. Scale bar: 5μm

Video 9. Arp2/3 complex is required to generate oscillatory motion of lateral E-cad clusters.
Live imaging of Ecad-GFP at a cell-cell contact in control or ArpC2 knockdown cells. Scale bar: 5μm

Video 10. Actin cables connecting E-cad clusters condense from a low intensity isotropic F-actin network.
Ecad-GFP (green) and TagRFP-T-UtrCH (F-actin, red) at a cell-cell contact (left) and F-actin only (center and right panels). Note that a low intensity isotropic F-actin network condenses into brighter F-actin cables connecting E-cad clusters. Scale bar: 5μm

Video 11. F-actin stabilization by jasplakinolide reduces oscillation of E-cad clusters.
Live imaging of Ecad-GFP at a cell-cell contact after 10 minutes of DMSO (control) or jasplakinolide treatment. Scale bar: 5μm

Video 12. Distinct apicolateral regions of F-actin stability at cell-cell contacts.
Time-lapse imaging of F-actin (GFP-UtrCH, hot cyan) at a cell-cell contact (left) and the corresponding heat map (right). The top region corresponds to the zonula adherens .Scale bar: 5μm

Video 13. N-WASP restrains oscillatory motion of apical E-cad clusters.
Ecad-GFP at a cell-cell contact of control or N-WASP knockdown cells. Note the pulsatile behaviour of apical E-cad in N-WASP knockdown cells. The apical and lateral regions of the cell-cell contact are labelled. Scale bar: 5μm

Video 14. Fusion with N-WASP$^{\Delta VCA}$ reduces oscillatory motion of lateral cadherin clusters.
Live cell imaging at cell-cell contacts on cells expressing either Ecad-GFP or Ecad-GFP-N-WASP$^{\Delta VCA}$. Scale bar: 5μm.

Video 15. Homophilic clustering of lateral E-cad persists at the interface of a presumptive extruding H-Ras^{V12} expressing cell, however the oscillatory motion of lateral clusters is reduced.
Live imaging of either a WT/WT or a WT/H-Ras^{V12} interface, where an Ecad-GFP (Green, Wild-Type or Transformed) cell is surrounded by Ecad-tdTomato (Red) expressing cells. Scale bar: 5μm